JGR Oceans

RESEARCH ARTICLE
10.1029/2020JC016452

Impact of Different Atmospheric Forcing Sets on Modeling Labrador Sea Water Production

Clark Pennelly[1] and **Paul G. Myers**[1]

[1]Department of Earth and Atmospheric Sciences, University of Alberta, Edmonton, AB, Canada

Key Points:

- Five NEMO simulations with different atmospheric forcing had average annual air–sea heat fluxes vary up to 12 W m^{-2} over the Labrador Sea
- The combination of air–sea and lateral buoyancy fluxes produced variations in stratification that impacted the convection depth
- Greater buoyancy loss promoted denser, but not more voluminous, Labrador Sea Water

Supporting Information:

- Supporting Information S1

Correspondence to:

C. Pennelly,
Pennelly@ualberta.ca

Citation:

Pennelly, C., & Myers, P. G. (2021). Impact of different atmospheric forcing sets on modeling Labrador Sea Water production. *Journal of Geophysical Research: Oceans*, *126*, e2020JC016452. https://doi.org/10.1029/2020JC016452

Received 27 MAY 2020
Accepted 11 JAN 2021

Abstract A numerical modeling sensitivity study is carried out within the Labrador Sea by varying the atmospheric conditions. From forcing NEMO simulations with five atmospheric products commonly used in ocean modeling (DFS5.2, ERA-Interim, CGRF, ERA5, and JRA55-do), we calculate the air–sea heat fluxes that occur over the Labrador Sea (2002–2015 annual-average net heat flux: −53.4, −51.0, −46.6, −58.5, and −47.9 W m^{-2}). With differences up to 12 W m^{-2} in net surface heat flux averaged over a central region of the Labrador Sea, each product supplied different atmospheric conditions. While the salinity-dependent surface buoyancy fluxes were similar across all simulation, differences between each simulation's solar and nonsolar heat flux led to significant changes in the level of stratification (up to 400 J m^{-3}), depth of the mixed layer (up to 300 m), and thickness of Labrador Sea Water (LSW; up to 300 m). Greater buoyancy loss from the Labrador Sea produced LSW with greater density. However, the production rate of LSW was not clearly affected by small changes in the surface buoyancy flux.

Plain Language Summary The Labrador Sea, between Canada and Greenland, experiences deep convection, a process where the ocean's surface is cooled to such a point that it becomes denser than the water beneath it, causing the surface layer to mix downwards. The overlying atmospheric conditions, such as wind speed, temperature, and humidity, strongly control this cooling. We carry out five ocean simulations to explore how small changes in atmospheric conditions influence the Labrador Sea. Our simulations show that atmospheric forcing which enhances the cooling of the Labrador Sea causes the deep water formed here to become denser. While a denser water mass is produced, we find that the volume of this water mass is not necessarily enhanced with the additional cooling.

1. Introduction

Situated within the North Atlantic subpolar gyre between eastern Canada and Greenland, the Labrador Sea (Figure 1(a)) routinely experiences intense air–sea forcing. Midlatitude cyclones frequently pass over the Labrador Sea. These winter storms, which often come from Canada, are cold and relatively dry. The underlying ocean releases heat to the atmosphere, cools, and becomes denser. This densification is crucial to the deep convection which occurs within the Labrador Sea (Lab Sea Group, 1998).

Two aspects are common across regions with deep convection: a weakly stratified basin and strong surface buoyancy loss (Lab Sea Group, 1998; Marshall & Schott, 1999). Cyclonic circulation, while not required for convection, helps keep the basin weakly stratified by doming isopycnals. Cold winter winds remove buoyancy, eroding the stratification, and promoting deep convection which can surpass 2,000 m (Yashayaev, 2007). However, even with substantial surface buoyancy loss, a significant freshwater layer at the surface can prevent convection from occurring (Böning et al., 2016; Gelderloos et al., 2012) as more buoyancy removal would be required than the atmosphere could provide. Furthermore, even with weak stratification, winter periods with relatively calm atmospheric conditions can result in limited convection (Lazier et al., 2002). The North Atlantic Oscillation (NAO; Hurrell, 1995) index, calculated from the pressure difference between the Icelandic Low and the Azores High, can give insight into the degree which the atmosphere removes buoyancy from the subpolar gyre (Yashayaev & Loder, 2016). A positive NAO phase is often associated with stronger winds than the usual climatology (Hurrell & Deser, 2010), enhancing the buoyancy loss from the ocean (R. G. Curry et al., 1998) and driving deep convection. A negative NAO phase is often associated with less buoyancy loss, reducing the vertical depth of convection. While the NAO index gives a useful measure

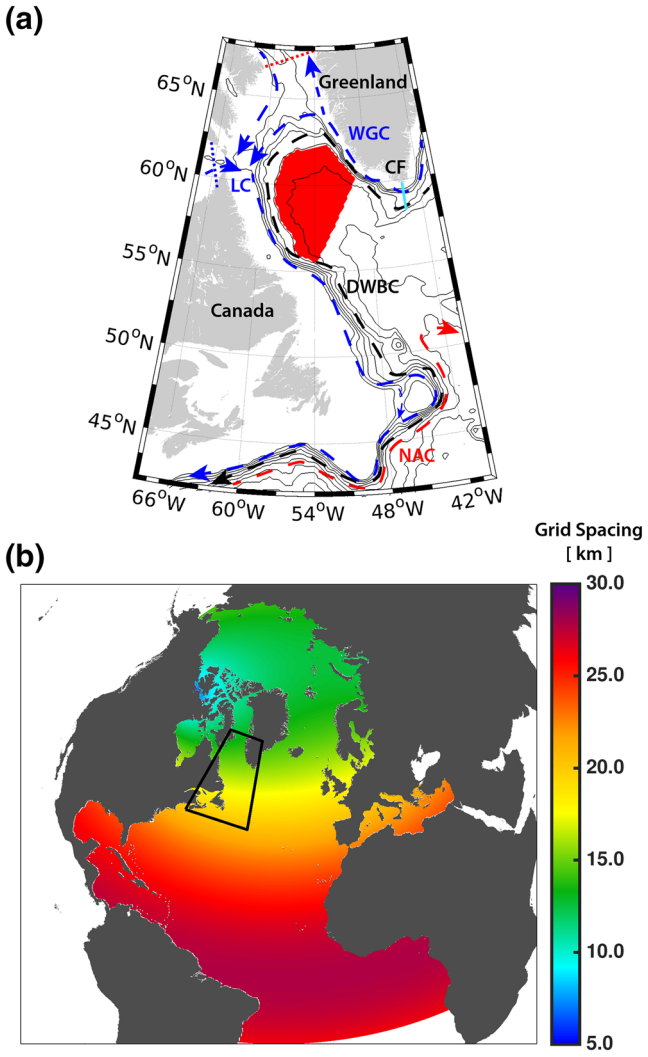

Figure 1. The Labrador Sea (a) with Davis (Hudson) Strait identified as the dotted red (blue) line. Isobath contour interval is 500 m. Dashed arrows are as follows: NAC is the North Atlantic Current, WGC is the West Greenland Current, LC is the Labrador Current, and DWBC is the Deep Western Boundary Current. The filled red polygon indicates our region of interest where analysis takes place. CF stands for our Cape Farewell section in teal. The ANHA4 configuration (b) is shown with colors indicating horizontal grid spacing (km) and the black box shows the spatial area covered in (a).

of the sea-level pressure anomaly, it does not guarantee conditions which promote significant air–sea heat loss (Moore et al., 2011) and deep convection in the Labrador Sea.

Deep mixing can occur with weak surface buoyancy loss if the stratification has been eroded sufficiently due to multiple successive years with strong convection (Pickart et al., 2002; Schulze et al., 2016). As it takes time for the stratification to rebuild, multiple years with strong buoyancy loss can produce a progressively thicker and denser Labrador Sea Water (LSW), leaving the basin weakly stratified for the following convection season (Lazier et al., 2002; Yashayaev & Loder, 2016). This occurred in the late 1980s to mid-1990s during a prolonged positive NAO phase with strong buoyancy loss, ultimately producing a thick layer of dense LSW (Yashayaev, 2007). If one uses NAO as a proxy for surface buoyancy loss, 1994 had the thickest LSW layer without the strongest forcing (Yashayaev, 2007). This implies that the buoyancy loss experienced during one convection period has lasting effects for the following year.

While the atmosphere removes buoyancy from the Labrador Sea, the boundary currents supply relatively buoyant water to restratify the region, steadily freshening the upper Labrador Sea while heating at depth (Straneo, 2006). This restratification process is strongly driven by the West Greenland Current (WGC) which carries fresh and cold water within the surface layer (0–200 m) and warm and salty Irminger Water within the subsurface layer (200–700 m: Chanut et al., 2008; Cuny et al., 2002; de Jong et al., 2016; Lazier et al., 2002; P. G. Myers et al., 2009; Rykova et al., 2015). The WGC and Labrador Current experience instabilities that produce buoyant eddies which make their way further offshore, bringing stratification into the interior Labrador Sea (Gelderloos et al., 2011; McGeehan & Maslowski, 2011; P. Myers, 2005; Pickart & Spall, 2007; Schmidt & Send, 2007; Spall, 2004). Wind-driven Ekman transport provides another route where freshwater within the boundary currents is able to travel toward the interior (Schulze & Frajka-Williams, 2018).

The combination of overlying stratification and significant surface buoyancy loss produces deep convection in the Labrador Sea, forming LSW, a water mass with a potential density between 1,027.68 and 1,027.80 kg m^{-3} (Kieke et al., 2006; Rhein et al., 2015; Yashayaev, 2007). LSW is one part of the lower limb within the Atlantic Meridional Overturning Circulation (AMOC). As the AMOC is part of the global thermohaline circulation, any changes within the Labrador Sea that modify the production of LSW may ultimately influence this global circulation. Turbulent heat and freshwater fluxes that control the stratification within the Labrador Sea were found to impact the AMOC (Yeager & Danabasoglu, 2014). As atmospheric forcing strongly controls these fluxes, uncertainty in atmospheric forcing may force simulations to be very different, as Pillar et al. (2018) found to occur within the AMOC transport within 15 years, primarily due to zonal winds and surface heat flux. However, the role of the Labrador Sea in relationship to the overturning circulation is an active area of research (Li et al., 2019; Lozier et al., 2019).

Much research has been carried out on how atmospheric forcing can impact the Labrador Sea. Holdsworth and Myers (2015) performed numerical simulations without the presence of midlatitude cyclones by filtering out high-frequency variability present within their forcing data and found that the absence of cyclones reduced the subpolar gyre and AMOC strength by about 25%. Garcia-Quintana et al. (2019) expanded upon this by performing a sensitivity study on the influence of LSW production by filtering storms as well as decreasing precipitation. They found that filtering storms reduced LSW volume production by

82%, primarily by producing a water mass with lighter density than LSW. Their simulation which reduced precipitation by 66% had the reverse response, producing a more voluminous water mass which was denser than LSW. Bramson (1997) showed that alterations in wind stress and precipitation induced changes within the mixed layer of the Labrador Sea. Chadhuri et al. (2016) forced an ocean model with various atmospheric forcing data sets, noting significant differences in the meridional overturning stream function that they attributed to variability in the wind stress or heat flux within the North Atlantic. Others have found that the location of wind may be more important than the frequency or strength of winds; Schulze et al. (2016) noted that the greatest heat loss was primarily due to the organization of the storm track. Moore et al. (2011) and Duvivier et al. (2016) note the importance of Greenland's strong tip jets on the surrounding seas, increasing the sensible and latent heat fluxes. Some suggest that the maximum surface heat loss is due to the location of the sea-ice edge (Marshall & Schott, 1999), although Moore et al. (2014) suggest that upstream and downstream topographies also influence the region of maximum turbulent heat loss.

While atmospheric forcing sets are useful for driving ocean simulations, they present other issues. Renfrew et al. (2002) found that these data sets may significantly deviate from observations within the Labrador Sea, suggesting simulations could be far from reality. The spatial and temporal resolution of atmospheric forcing data sets determines the scale of features that are included. Lower-resolution data sets may fail to properly resolve mesoscale features that strongly impact the surface heat flux (Condron & Renfrew, 2013; Jung et al., 2014) that is vital to controlling the stratification and deep convection within the Labrador Sea.

Long-term climate simulations (100+ years) often use low resolution (approximately 1/4° and coarser) to investigate future scenarios and situations (IPCC, 2014). These simulations help us understand and form policy on a changing climate even though they misrepresent some aspects. Deep convection, within both the atmosphere and ocean, occurs at a much smaller scale (<1 km) than these simulations can resolve. To fully resolve deep convection, ocean simulations require very high resolution (Raasch and Etling [1997] had success with 25 m) and nonhydrostatic physics. The computing requirements for such a coupled climate simulation that spans 100+ years are not feasible. However, numerical modelers have long since been able to work around these subgrid-scale features by adding parameterizations to their code that mimic the effects while not resolving the features. This allows for ocean simulations of any resolution to include the effects of deep convection while not physically resolving it.

Here, we explore how the buoyancy fluxes associated with numerous atmospheric forcing products influence the formation rate and density of LSW. We investigate this by using five different atmospheric forcing products to drive a 1/4° eddy-permitting ocean simulation. We explore the differences between the different products as well as the ocean's response when driven by each product. While we do not explicitly resolve convection, our objective is to quantify how small differences in surface forcing influence an area where deep water is formed. This is particularly relevant for a suite of simulations that differ in their atmospheric forcing; for example, the Representative Concentration Pathways simulations (Van Vuuren et al., 2011).

2. Methods

To investigate the differences in atmospheric forcing on LSW formation, we chose to use different atmospheric forcing data sets used by the ocean modeling community rather than carry out sensitivity simulations by perturbing a single forcing set away from its original state. Such perturbations may identify the sensitivity of LSW formation on select aspects (e.g., Bramson, 1997; Garcia-Quintana et al., 2019) but perturbation simulations may no longer carry a realistic imprint of the surface forcing. To keep our simulations as realistic as possible, we examined five different atmospheric forcing data sets: ERA-Interim (Dee et al., 2011), Drakkar Forcing Set 5.2 (DFS5.2; Dussin et al., 2016), Canadian Meteorological Centre's Global Deterministic Prediction System Reforecasts (CGRF; Smith et al., 2014), ERA5 (Hersbach & Dee, 2016), and the Japanese Reanalysis product JRA55-do (Tsujino et al., 2018).

Each atmospheric data set provides near-surface conditions to force ocean simulations. These data sets differ from one another (Table 1) in spatial/temporal resolution, reference height for data fields, as well as the type of product. We do not investigate how these differences influence the surface buoyancy flux provided by each data set. However, others have noted that higher spatial resolution produces a larger

Table 1
Information Regarding Each Atmospheric Forcing Data Set Used to Force the Simulations

Data set	Spatial resolution (km)	Temporal resolution (h) (wind/temperature/ precip/radiation)	Temperature and moisture height (m)	Wind speed reference height (m)	Years of coverage	Product type
ERA-Interim	45	3/3/24/24	2	10	1979+	Reanalysis
DFS 5.2	45	3/3/24/24	2	10	1958–2015	Reanalysis
CGRF	33	1/1/1/1	2	10	2002+	Reforecast
ERA5	30	1/1/1/1	2	10	1979+	Reanalysis
JRA55-DO	31	3/3/3/3	10	10	1958+	Reanalysis

Note. Spatial resolution is the average grid spacing over the red polygon in the Labrador Sea (Figure 1(a)).

variance in the wind speed and heat flux (Brossier et al., 2012; Jung et al., 2014; Langlais et al., 2009) while higher temporal resolution helps resolve the diurnal heating that stratifies the upper ocean and mesoscale features (Brossier et al., 2012). Differences in the reference height indicate a slightly different method to calculate the drag transfer coefficient (Equations 1 and 2; Large & Yeager, 2008), influencing the air–sea transport of momentum, freshwater, and heat. CGRF, the only reforecast product, stitches together daily forecasts to produce the final product. The authors of CGRF (Smith et al., 2014) even state that CGRF "... is not a reanalysis and thus is expected to be less well constrained by available observations," but highlight its high resolution and relatively small bias. As each data set was produced using a different numerical framework, readers should refer to the documentation listed above for further information regarding each data set. It should be noted that each of these forcing sets has been used in ocean hindcast simulations (e.g., ERA-Interim: Lindsay et al., 2014; DFS5.2: Benetti et al., 2017; CGRF: Gillard et al., 2016; ERA5: Wilson et al., 2019; and JRA55-do: Tsujino et al., 2018). Each atmospheric data set was used to force a numerical simulation as detailed below.

All simulations had the NEMO ocean model version 3.4 (Madec, 2008) coupled with the LIM2 sea-ice model (Fichefet & Maqueda, 1997). Each simulation used the regional 1/4° horizontal resolution Arctic and Northern Hemisphere Atlantic (ANHA4; Figure 1(b)) configuration (Courtois et al., 2017; Holdsworth & Myers, 2015; Müller et al., 2017) with 50 vertical levels and open boundaries across Bering Strait and 20°S. Initial and open boundary conditions were obtained from the global 1/4° GLORYS2v3 simulation (Ferry et al., 2010). Interannual monthly runoff was a combination of Dai et al. (2009) as well as Greenland derived liquid runoff via a surface mass balance model (Bamber et al., 2012). While atmospheric products may include their own runoff data, we opted to keep this freshwater source constant between the simulations; see Gillard et al. (2016) or Garcia-Quintana et al. (2019) on how the Labrador Sea is impacted by changes in runoff. Other than the prescribed atmospheric state, all simulations had identical settings and no restoring was performed on any simulation. We name each simulation by the atmospheric forcing product used, though we also shorten some of the names for brevity. Henceforth, the simulation which used the DFS5.2 data set is known as DFS, ERA-interim as ERA, CGRF as CGRF, ERA5 as ERA5, and JRA55-do as JRA. Each simulation was initialized at the start of the year 2002 and continued until the end of 2015. No spin-up was performed as the initial conditions from GLORYS2v3 (Ferry et al., 2010) already had about 1 decade of integration since initialization.

All simulations used the CORE bulk formulae for the heat, momentum, and freshwater flux between the atmosphere and the ocean (Large & Yeager, 2008). Sensible (Equation 1) and latent (Equation 2) turbulent heat fluxes are determined from the humidity, temperature, and velocity difference between the ocean's surface and the overlying atmosphere. Positive values indicate a heat flux from the atmosphere into the ocean. Equation variables are as follows: C is the specific heat of air at 1,000.5 J kg^{-1} K^{-1}, ρ is the density of air at 1.22 kg m^{-3}, T_o is the ocean's surface temperature in degrees Kelvin, T_a is the potential air temperature in degrees Kelvin, L_v is the latent heat of vaporization (2.5×10^6 J kg^{-1}), q_o is the specific humidity (kg kg^{-1}) of 100% saturated air with a temperature equal ocean's surface, q_a is the specific humidity (kg kg^{-1}) of the air at 10 m height, U_{ao} is the relative wind speed compared to the ocean's surface in m s^{-1}, while C_h and C_e are sensible and latent transfer drag coefficients (see Large & Yeager, 2008).

$$\text{Sensible turbulent heat flux} = C\rho C_h\left(T_a - T_o\right)U_{ao} \tag{1}$$

$$\text{Latent turbulent heat flux} = \rho C_e L_v\left(q_a - q_o\right)U_{ao} \tag{2}$$

The various air–sea heat fluxes accumulate to produce a change in the temperature, and thus density, of the ocean's surface. However, each atmospheric forcing product also contains precipitation and snow which not only influences the sensible and latent heat fluxes but also contributes to the surface buoyancy flux via the addition of freshwater. To explore these effects, we examine both the air–sea heat fluxes as well as the net surface buoyancy flux (see Sathiyamoorthy & Moore, 2002).

To help illustrate the differences that atmospheric forcing products have on LSW production, we examine various diagnostics of the Labrador Sea. To calculate the stratification strength, convective energy is used (our Equation 3; Holdsworth & Myers, 2015). Convective energy is the amount of energy needed to be removed such that the water column is neutrally stratified to some reference depth. The convective energy to a reference depth, h, is calculated as

$$\text{Convective energy}\left(h\right) = \frac{g}{Area}\iint\left[h\,\rho_\theta\left(h\right) - \int_0^h \rho_\theta\left(z\right)dz\right]dA \tag{3}$$

where g is the gravitational constant, $Area$ is the total surface area of our region of interest (Figure 1(a)), $\rho_\theta(z)$ and $\rho_\theta(h)$ are the potential density at each grid cell and the potential density of the grid cell at the reference depth, and A is the surface area of each grid cell. Positive convective energy indicates stable stratification while negative values indicate unstable stratification. We selected a reference depth of 2,000 m as convection can reach this depth (Yashayaev, 2007).

While convective energy indicates the degree of stratification, it does not provide any information on the depth of the mixed layer. One calculation of the mixed layer depth (MLD) is a 0.01 kg m^{-3} deviation between the potential density at the surface and that of the bottom of the mixed layer. For shallow regions, this appears to work fine, but falters for regions with deep convection (Courtois et al., 2017) as temperature and salinity can compensate to keep the density uniform while the water column properties are no longer well mixed. To remedy this, we implemented a method (see Courtois et al., 2017) based on Holte and Talley (2009) which examines the water column to estimate the MLD based on the linear interception of the thermocline and the mixed layer as determined by a 0.01 kg m^{-3} change in potential density from the surface. The final MLD is the minimum of this intersection or the value found using the 0.01 kg m^{-3} difference in potential density method. This was carried out during all numerical simulations as well as on the observations from Argo floats.

The mixed layer alone does not provide enough information to determine the production volume of LSW as water can leave and enter the mixed layer in multiple ways. Production of LSW is determined via a kinematic subduction approach (our Equation 4; see Feucher et al., 2019; Garcia-Quintana et al., 2019). We use this approach to bin the total water mass which moves through the mixed layer by density class (1,023.0–1,028.4 kg m^{-3}) per year (τ), with density bins of 0.01 kg m^{-3} width. Water may enter and leave the mixed layer (Z_σ) via lateral advection ($v \cdot \nabla h$), vertical advection (W_b), as well as when the mixed layer changes depth ($\partial h/\partial t$).

$$\text{Subduction} = \frac{-1}{\tau}\int_0^\tau \int_{A_\sigma}\left[W_b + \frac{\partial h}{\partial t} + v \cdot \nabla h\right]dZ_\sigma\, dt \tag{4}$$

Subduction identifies the total amount of LSW that was produced within a certain density class, though does not give information on the thickness of LSW. As mentioned above, LSW can be classified by density. Due to salinity-driven density drift of our model simulations, a common issue for numerical simulations in the Labrador Sea (Marzocchi et al., 2015; Rattan et al., 2010), we had to alter our definitions of LSW. Instead of defining LSW using a density criteria between 1,027.68 and 1,027.80 kg m^{-3} (see Kieke et al., 2006; Rhein et al., 2015; Yashayaev, 2007), we allowed the classification to change in time based on the results from each simulation (see below, Figure 10). Others have had success by classifying LSW that evolves in time to

compensate for model drift; Feucher et al. (2019) investigated the link between LSW and Meridional Overturning Circulation. Our calculation of the density of LSW closely follows their approach which is based on observations of LSW that change in time. First, we calculated the yearly subduction (Equation 4) rate binned by density (bin width 0.01 kg m^{-3}); the densest bin with positive subduction was used to determine the density of LSW. Our LSW classification is defined from the greatest density within this 0.01 density bin to a minimum density 0.12 kg m^{-3} lighter; the 0.12 kg m^{-3} comes from the traditional density range of LSW (see above). We then divided LSW into two equal parts to produce a denser modified Classical Labrador Sea Water (CLSW) and less dense Upper Labrador Sea Water (ULSW); the midpoint between our LSW density range was where ULSW transitioned into CLSW. This was done for every simulation year and linearly smoothed between years to prevent any step jumping from occurring. Simulations will likely not have the same density drift due to changes in surface forcing and resulting lateral fluxes. This method forced the production of deep water within the Labrador Sea to be classified as LSW despite any numerical drift which occurred. Other methods at classifying LSW were attempted, but the one described above best captured the interannual variability of ULSW and CLSW.

As heat and freshwater contribute to setting the stratification in the Labrador Sea, we calculate the westward heat and freshwater transport across a section which extends from Cape Farewell to the 2,500 m isobath (CF: Figure 1(a)). This is done for both water masses within the current system: cold and fresh ($S < 34.8$, $\rho_\theta < 1{,}027.68$ kg m^{-3}) East Greenland Current (EGC) water and warm salty Irminger Water ($T > 3.5$°C, $S > 34.8$, $\rho_\theta < 1{,}027.68$ kg m^{-3}). Temperatures and salinities were chosen to be consistent with others who have investigated these water masses in the past (Kieke et al., 2006; P. G. Myers et al., 2007), although we also imposed a density criteria to prevent classification of water which might be LSW using a classical, non-drift density definition (see above).

To evaluate our simulations, we compare against data from Argo floats (http://www.argo.net). Argo float's temperature and salinity data are used to determine the MLD using the method outlined by Holte and Talley (2009) that works well for areas with deep convection (Courtois et al., 2017). Comparison against Argo data, as well as the above proxy calculations, took place over the red region of interest in Figure 1(a). This region is the area between the 2,500 m isobath and Atlantic Repeat Hydrography Line 7 West and was chosen as deep convection occurs over a large part of this region in our 1/4° simulations. While this region is larger than the observed convective region (see Yashayaev & Loder, 2016), the convective region remains too spacious in models even with 1/12° horizontal resolution (Courtois et al., 2017). Lengthy low-resolution climate simulations that investigate perturbations in forcing likely suffer as well. As our goal is to investigate how differences in surface forcing impact deep water produced within the Labrador Sea, our findings should be pertinent for certain climate simulations.

3. Results

3.1. Atmospheric Variability Over the Labrador Sea

Before we investigate the Labrador Sea's response to each of the five atmospheric forcing data sets, we first quantify the differences between the data sets. Figure 2 shows the 2002–2015 average daily precipitation and wind speed for the five atmospheric forcing data sets. DFS5.2 (Figure 2(a)) and ERA-Interim (Figure 2(b)) are very similar, primarily as DFS5.2 is built from ERA-Interim. JRA55-do (Figure 2(e)) has less precipitation around Greenland than the others. CGRF (Figure 2(c)) has less precipitation in and around the tropics and the Labrador Sea, with JRA55-do having slightly more, whereas ERA5 (Figure 2(d)) has most precipitation. Wind speed appears very similar across the North Atlantic for these forcing sets. While these forcing sets have differences across the North Atlantic, we now focus within the Labrador Sea.

Figure 3 illustrates the (a) shortwave radiation, (b) longwave radiation, (c) near-surface temperature, (d) near-surface specific humidity, (e) precipitation, and (f) 10-m wind speed for each of the five data sets as spatially averaged across the red polygon in Figure 1(a), a region where the model simulations contain deep convection. Data were averaged across each month from 2002 to 2015 to construct these box and whisker plots. While this figure graphically illustrates that there are differences between each data set, Table 2 quan-

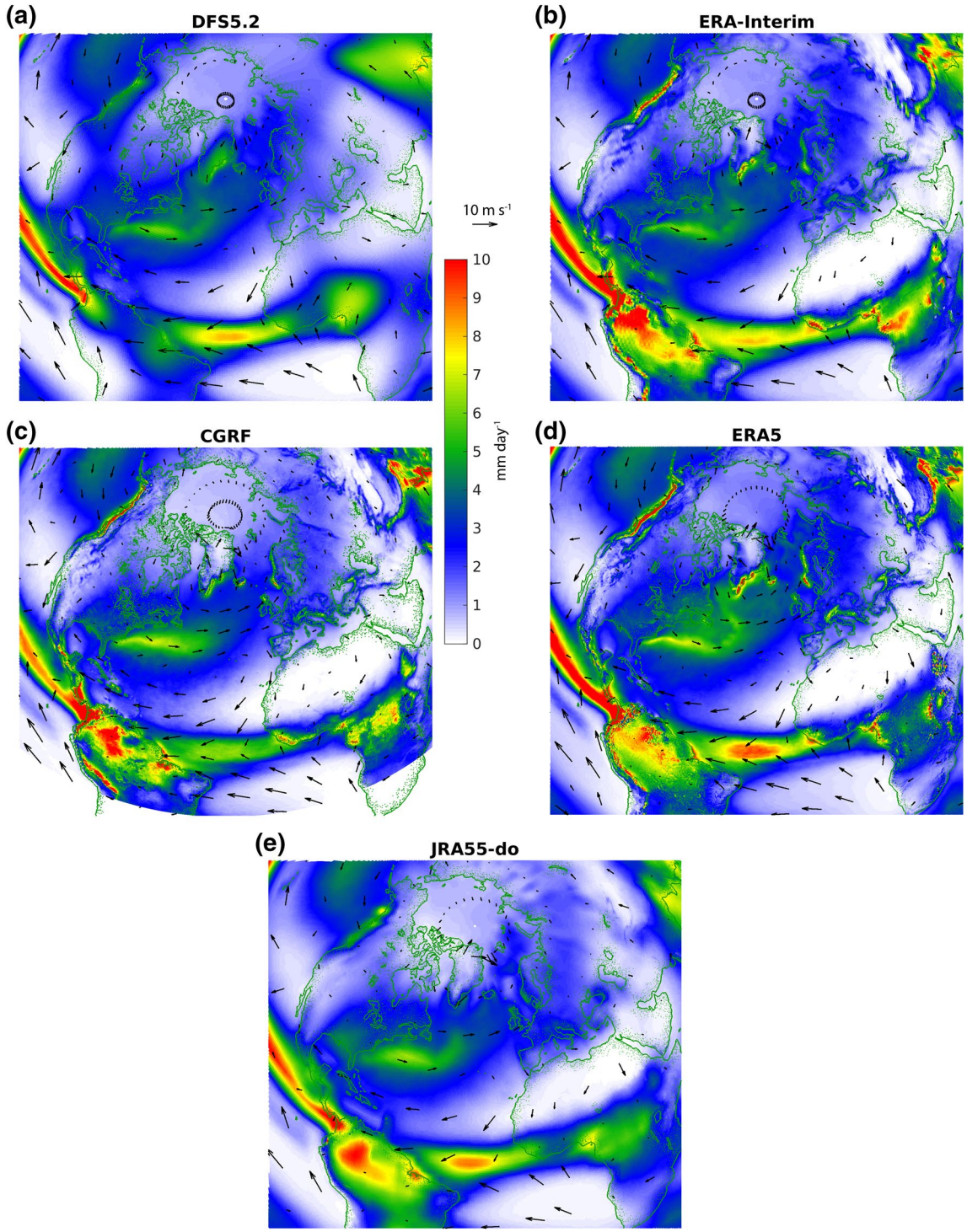

Figure 2. Average daily precipitation (contours; mm day^{-1}) and wind velocity (barbs; m s^{-1}) from 2002 through the end of 2015 for each of our atmospheric forcing data sets. Wind barbs were selectively displayed to preserve visual quality and do not represent spatial resolution; see Table 1 for more details.

tifies the 2002–2015 mean and standard deviation. As each of these six atmospheric variables influences the surface buoyancy flux, we will describe the variability present in Figure 3 and Table 2.

JRA55-do has the lowest average shortwave radiative heat flux (Figure 3(a); 89.9 W m^{-2}) with CGRF slightly higher (93.7 W m^{-2}). While both of these data sets have the least incoming shortwave radiation, they also

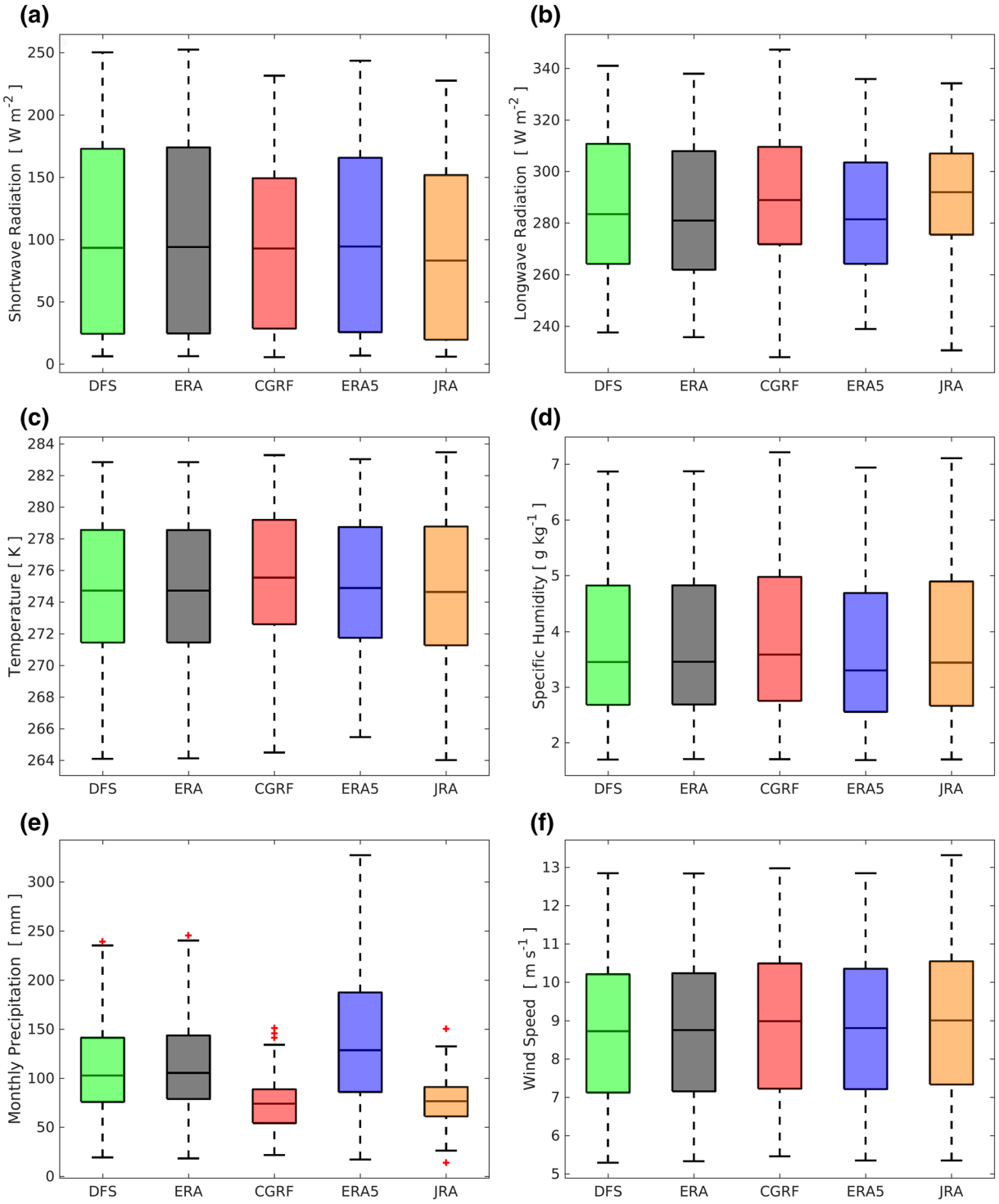

Figure 3. (a) Downward shortwave radiation, (b) downward longwave radiation, (c) temperature, (d) specific humidity, (e) precipitation, and (f) wind speed as supplied by the five atmospheric data sets. Values were spatially and temporally averaged each month from 2002 to 2015 over the red polygon in Figure 1(a). Colored boxes indicate the interquartile range. Whiskers lengths are, at most, 150% of the interquartile range while red crosses indicate outliers. The horizontal black line within the colored rectangles indicates the median.

Table 2
2002–2015 Average Yearly Atmospheric Conditions as Supplied by Each Atmospheric Data Set to the Red Polygon in Figure 1(a)

Atmospheric forcing data set	Shortwave radiation (W m^{-2})	Longwave radiation (W m^{-2})	Temperature (K)	Specific humidity (g kg^{-1})	Precipitation (mm)	Wind speed (m s^{-1})
DFS5.2	103.6 (78.7)	286.7 (28.2)	274.7 (4.4)	3.8 (1.3)	110.4 (47.4)	8.7 (1.7)
ERA-Interim	104.4 (79.3)	284.1 (27.9)	274.7 (4.3)	3.8 (1.3)	112.6 (26.1)	8.7 (47.8)
CGRF	93.7 (65.8)	290.5 (25.2)	275.7 (4.1)	3.9 (1.4)	73.7 (26.2)	8.8 (1.7)
ERA5	99.5 (72.6)	283.4 (24.9)	274.9 (4.4)	3.7 (1.4)	141.2 (69.3)	8.8 (1.7)
JRA55-DO	89.9 (67.8)	289.2 (23.8)	274.9 (4.6)	3.8 (1.4)	77.3 (22.2)	9.0 (1.8)

Note. Numbers inside the parentheses indicate one standard deviation.

tend to have higher longwave radiation values (Figure 3(b); JRA55-do: 289.2 W m^{-2}; CGRF: 290.5 W m^{-2}) compared to the remaining data sets. Combining radiative heat fluxes show that the DFS5.2 (390.3 W m^{-2}) and ERA-Interim (388.5 W m^{-2}) sets are similar while CGRF (384.2 W m^{-2}), ERA5 (382.9 W m^{-2}), and JRA55-do (379.1 W m^{-2}) provide less heat via radiation.

Near-surface temperature (Figure 3(c)) and specific humidity (Figure 3(d)) show that the CGRF simulation is the warmest (275.7 K) and most humid (3.9 g kg^{-1}). The remaining data sets have nearly the same mean temperature (274.7–274.9 K). ERA5 has the least humidity (3.7 g kg^{-1}) while ERA-Interim, DFS5.2, and JRA55-do have nearly the same (3.8 g kg^{-1}).

Monthly precipitation (Figure 3(e)) is rather different between the data sets, with ERA5 having a mean of 141.2 mm while JRA55-do and CGRF have the least (77.3 and 73.7 mm). DFS5.2 and ERA-Interim had nearly the same monthly precipitation (110.4 and 112.6 mm). Whisker plots of the monthly average wind speeds (Figure 3(f)) show that the JRA55-do forcing has the strongest wind (9.0 m s^{-1}) while the others are nearly the same (8.7–8.8 m s^{-1}).

These small differences in surface forcing affect the Labrador Sea in multiple ways. Radiative fluxes increase the temperature of the ocean's surface, increasing stratification. The near-surface temperature and specific humidity influence not only the latent and sensible heat fluxes that deal with evaporation but also the turbulent heat fluxes that wind speed influences. Precipitation supplies both a freshwater source that modifies the surface buoyancy flux and sensible/latent heat fluxes as well. The following section examines NEMO simulations that are driven by these atmospheric forcing data sets and the resulting changes within the Labrador Sea.

3.2. Model Evaluation

The ANHA4 configuration has been evaluated within the North Atlantic in numerous studies (see Courtois et al., 2017; Garcia-Quintana et al., 2019; Gillard et al., 2016; Holdsworth & Myers, 2015; Müller et al., 2017), though we provide additional evaluation as it pertains to our research questions. Before investigating LSW production from the ANHA4 simulations, we first seek to determine if each simulation is representing reality to some acceptable level. To do this, we compare the volume, heat, and freshwater flux (Table 3) through Davis and Hudson Strait (see Figure 1(a)) to determine the fluxes into the Labrador Sea. First, all simulations had nearly the same volume transport through Hudson Strait, with about 0.08–0.09 Sv of net transport toward the Labrador Sea in agreement with Drinkwater's (1988) and Straneo and Saucier's (2008a) estimates of between 0.08 and 0.1 Sv. Davis Strait has much higher flow, around 1.6 ± 0.5 Sv (B. Curry et al., 2014), vastly outweighing that of Hudson Strait. The ERA and DFS simulations (1.74 and 1.76 Sv) most closely matched the observed transport while JRA was higher (2.02 Sv). The CGRF simulation was the only one to have less volume transport (1.3 Sv) than observations suggest. All simulations were within a standard deviation of the observed volume transport across Davis Strait.

The net freshwater flux across Hudson Strait, using a salinity reference of 34.8, is 35 mSv (ERA), 34 mSv (JRA), 32 mSv (ERA5), 31 mSv (CGRF), and 28 mSv (DFS). As our simulations use the same runoff forcing, these freshwater transport differences arise from a combination of precipitation minus evaporation and cir-

Table 3
Observed and Model Calculated Volume, Freshwater (Referenced to 34.8), and Heat (Referenced to 0°C) Flux Through Hudson and Davis Strait From 2004 to 2011, the Same Period as the Observation Moorings Across Davis Strait

		Observations	DFS	ERA	CGRF	ERA5	JRA
Volume (Sv)	Hudson	0.1[a,b]	0.09	0.09	0.08	0.09	0.09
	Davis	1.6 ± 0.5[c]	1.76	1.74	1.30	1.86	2.02
Freshwater (mSv)	Hudson	40[b,d]	28	35	31	32	34
	Davis	100[c]	108	116	78	124	116
Heat (TW)	Hudson		0.1	0.1	0.1	0.1	0.1
	Davis	-20[e]	-18	-22	-25	-21	-23

Note. Positive values indicate equatorward flux.
[a]Drinkwater (1988). [b]Straneo and Saucier (2008a). [c]B. Curry et al. (2014). [d]Dickson et al. (2007). [e]B. Curry et al. (2011).

culation changes. Determining the relative strength of each factor was outside the scope of this manuscript. Ridenour et al. (2019) explored freshwater within the Hudson Bay Complex via numerical simulations that had varying runoff forcing. Both our study and Ridenour et al. (2019) had lower freshwater transport through Hudson Strait than observed (40 mSv: Dickson et al., 2007; Straneo & Saucier, 2008a). Freshwater flux through Davis Strait, observed to have a southwards transport of about 100 mSv (B. Curry et al., 2014), is in agreement with our results which had between 78 mSv (CGRF) and 124 mSv (ERA5). While the heat flux leaving Hudson Strait has been investigated (Straneo & Saucier, 2008a, 2008b), net heat flux estimates are lacking. However, our numerical simulations suggest that the net heat flux is very small (0.1 TW) when compared against the neighboring Davis Strait which compares well with observations (20 TW: B. Curry et al., 2011) as our simulations held between 18 TW (DFS) and 25 TW (CGRF) of poleward heat transport.

With reasonable fluxes through both Davis and Hudson Strait, the northern gateways into the Labrador Sea are adequately simulated. However, eddies known as Irminger Rings (Chanut et al., 2008) spawn along the west coast of Greenland and travel into the interior of the Labrador Sea, bringing relatively buoyant water. A comparison of the eddy kinetic energy $\left(\text{EKE}:0.5\left(\overline{U_g'^2}+\overline{V_g'^2}\right)\right)$, where U_g' and V_g' are the geostrophic velocities computed from the sea surface height anomaly, is carried out between our five simulations and AVISO observations (Figure 4). While all simulations show similarities, they do not capture the high EKE southwest of Greenland or within the Northwest Corner near Newfoundland, Canada. Much of this can be attributed to the ¼° horizontal resolution used by the model; these simulations are not eddy resolving in this region but rather eddy permitting. EKE across the simulations is very similar except for perhaps CGRF which has higher EKE in the western Labrador Sea. Thus, eddy fluxes would be similar across these simulations unless there are changes within the boundary currents—we explore this later below. While the differences in simulated EKE and eddy fluxes into the interior of the Labrador Sea will be different than observed, the resolution used should suffice for understanding how differences in air–sea heat flux contribute to changes in the volume and density of LSW produced during convection. As modern long-term climate simulations have comparable horizontal resolution and likely also suffer from reduced eddy fluxes in this region, the results we present should be of interest to the climate modeling community.

3.3. Heat Fluxes

With acceptable representation through the gateways of the Labrador Sea, we can investigate how the Labrador Sea responds to different atmospheric forcing. First, we consider the monthly air–sea heat fluxes (Figure 5). The top row indicates the sensible heat fluxes determined by turbulent process within our region of interest (Figure 5(a)), sensible heat flux from rainfall (Figure 5(b)), and sensible heat flux from snowfall (Figure 5(c)). One can quickly identify that the sensible heat flux is dominated by turbulent processes with monthly values that range from an input of nearly 10 W m^{-2} to a release of about 90 W m^{-2}. Rainfall and snowfall provide and remove a sensible heat flux of order 1 W m^{-2}.

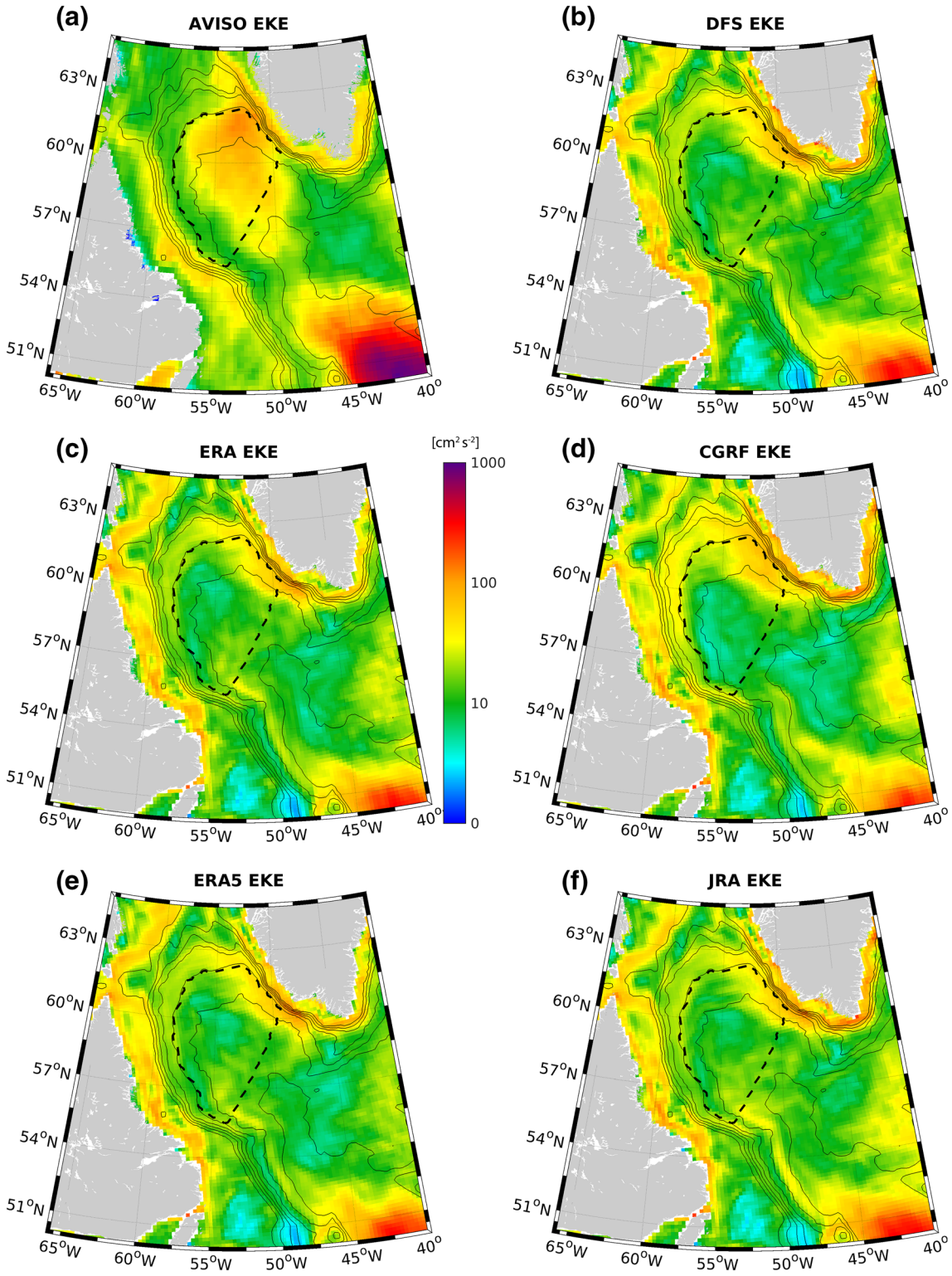

Figure 4. Eddy kinetic energy (EKE, in $cm^2\ s^{-2}$) from 2004 to 2015 as derived from AVISO observations (a) as well as the five model simulations (b–f). The black dashed line indicated the region of interest (Figure 1(a)).

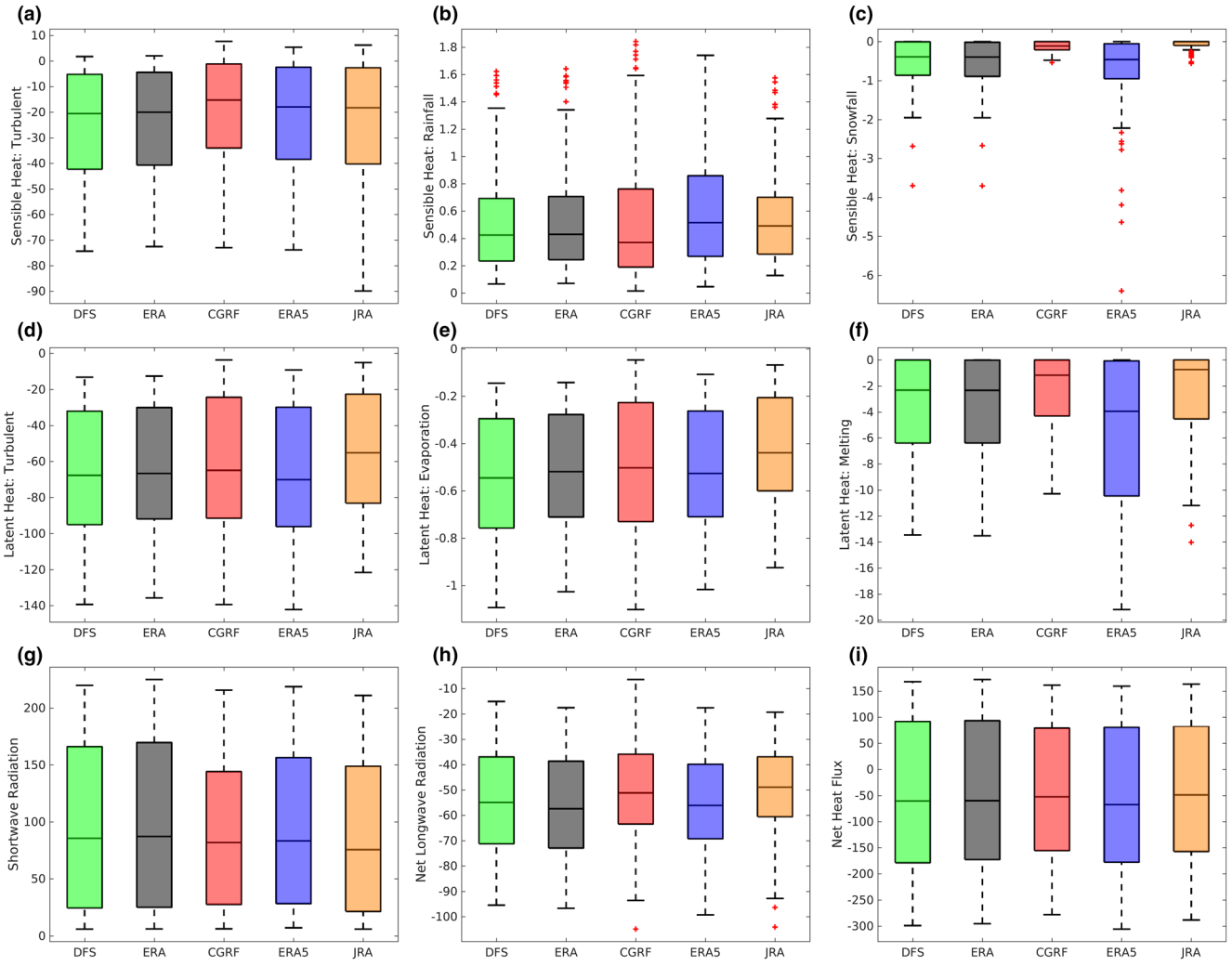

Figure 5. Spatially averaged (red polygon, Figure 1(a)) monthly air–sea heat fluxes (W m^{-2}) to the Labrador Sea from 2002 to 2015. Sensible heat from (a) turbulent motion, (b) rain, and (c) snow is shown in the top row. Latent heat from (d) turbulent motion, (e) evaporation, and (f) melt of snow is shown in the middle row. Radiative heating is shown for the net shortwave radiation (g) and net longwave radiation (h). All fluxes combine to produce the net air–sea heat flux (i). Whiskers lengths are, at most, 150% of the interquartile range while red crosses indicate monthly outliers.

The middle row of Figure 5 illustrates the latent heat flux via turbulent processes (Figure 5(d)), evaporation (Figure 5(e)), and melting of snowfall (Figure 5(f)). Evaporation occurs where there exists any difference in specific humidity between the air just above the ocean, calculated from the ocean's surface temperature with a relative humidity of 100%, and the air as supplied by the forcing products at 10 m above sea level. Turbulent heat flux is greatly influenced by the speed difference between the ocean and atmosphere (Equation 2) but still requires a difference in specific humidity. The heat fluxes via latent processes remove more heat than sensible processes (Table 4) in this region. Turbulent latent heat fluxes, when averaged across each year (-5 to -140 W m^{-2}), remove much more heat than is associated with the evaporation of water (-0.1 to -1.1 W m^{-2}) and melting of snowfall (0 to -19 W m^{-2}).

The bottom row of Figure 5 illustrates the net radiative fluxes (shortwave, Figure 5(g); longwave, Figure 5(h)) as well as the net air–sea heat flux (Figure 5(i)). The shortwave radiative heat flux is slightly reduced compared to the input (Figure 3(a)) due the albedo at the ocean's surface, a constant value set at 0.066 within NEMO. When all air–sea heat fluxes are accounted for (Figure 5(i)), we see small differences between data sets. However, examination of the long-term air–sea fluxes (Table 4) shows that the CGRF simulation releases the least heat (46.6 W m^{-2}) compared to the others, with JRA close behind (47.9 W m^{-2}). ERA, DFS, and ERA5 show heat losses of 51.0, 53.4, and 58.5, W m^{-2}, respectively. Both Table 4 and Figure 5

Table 4
Average Heat Flux (W m^{-2}) From 2002 to 2015 for the Five Simulations as Calculated Within the Red Polygon in Figure 1(a)

	Net downward		Sensible heat flux			Latent heat flux			
Simulation	Shortwave	Longwave	Snowfall	Rainfall	Turbulent	Melt	Evaporation	Turbulent	Total
DFS	97.3 (80.4)	−54.5 (29.4)	−0.5 (2.2)	0.5 (0.9)	−26.1 (31.5)	−3.6 (5.8)	−0.5 (0.4)	−66.0 (52.8)	−53.4
ERA	99.1 (81.8)	−56.4 (29.0)	−0.5 (2.3)	0.5 (0.9)	−25.2 (31.0)	−3.6 (5.8)	−0.5 (0.4)	−64.4 (51.6)	−51.0
CGRF	88.9 (137.6)	−50.1 (32.8)	−0.1 (0.5)	0.5 (1.3)	−19.7 (28.3)	−2.3 (6.3)	−0.5 (0.4)	−63.3 (55.5)	−46.6
ERA5	95.4 (148.1)	−56.2 (29.2)	−0.7 (4.0)	0.6 (1.2)	−23.6 (32.2)	−5.8 (10.5)	−0.5 (0.4)	−67.7 (56.1)	−58.5
JRA	87.3 (132.3)	−50.9 (30.5)	−0.1 (0.2)	0.5 (1.0)	−24.9 (35.6)	−2.7 (5.2)	−0.4 (0.4)	−56.7 (51.2)	−47.9

Note. Positive values indicate a supply of heat to the Labrador Sea. Numbers within the parentheses indicate one standard deviation.

identify that the primary heat fluxes are via radiation and turbulent processes; the nonturbulent sensible and latent heat fluxes combine to remove a small amount of heat, between 3.4 and 7.7 W m^{-2}. The turbulent heat fluxes (Equations 1 and 2) arise from the difference between the temperature, humidity, and speed of the ocean and the overlying atmosphere (S1).

The change in oceanic heat content is shown in Figure 6(a). Winter periods are shown from the yearly minimums, driven by the air–sea heat losses described above, while summer periods experience a heat gain. Summer maximums do not deviate much from one another (up to 100 W m^{-2}) although there is considerable spread across the winter minimums (up to about 350 W m^{-2}). This spread can be explained by the changes in air–sea heat loss as 2010 had very weak loss while 2008, 2012, and 2015 had much greater loss (our supplemental Figure S2(i); Yashayaev & Loder, 2017). As the long-term average in the oceanic heat content change is positive, all simulations have a gradual warming of the Labrador Sea. With long-term cooling of the ocean via air–sea heat fluxes (Table 4), lateral advection, calculated from the change in oceanic heat content and air–sea heat flux, supplies this heat (Figure 6(b)). We note that the variability in heat content is strongly linked to the air–sea heat fluxes (S2i) with correlation coefficients between 0.95 and 0.97. Lateral advection correlation coefficients are lower, between 0.78 (ERA) and 0.87 (JRA). The DFS simulation encountered the largest heat flux via lateral advection (83.9 W m^{-2}) while also having the second highest surface heat loss (-53.4 W m^{-2}). ERA, CGRF, JRA, and ERA5 supply less heat via lateral advection: 74.3, 73.1, 70.0, and 69.1 W m^{-2}, respectively.

The likely candidates for this heating are the boundary currents around the Labrador Sea, specifically the warm Irminger Water layer within the WGC. As varying the atmospheric conditions do not only impact the Labrador Sea, we investigate this current system upstream to understand the differences in the above lateral heat fluxes. Figure 7(a) shows the westward heat transport within the Irminger Water layer ($T > 3.5$°C, $S > 34.8$, $\rho_\theta < 1{,}027.68$ kg m^{-3}) extending south from Cape Farewell to the 2,500 m isobath (teal line, Figure 1(a)). While all simulations show similar interannual variability, the magnitudes are quite different; CGRF often transports the most heat within this water mass while the DFS and JRA simulations transport the least. However, as expressed above, the DFS simulation has the largest lateral heat flux while having low heat transport at the southern tip of Greenland for this water mass. Differences in the amount of heat and freshwater transport (discussed below) across this section are likely due to a combination of many factors, including but not limited to circulation changes in the Arctic and North Atlantic gyre, wind-stress curl and related Ekman pumping, Atmospheric oscillation modes, changes in sea ice, and differential heating/cooling. It is outside the scope of this manuscript to document how various atmospheric forcing data sets influence the oceanic conditions outside the Labrador Sea, although these factors produce slightly different conditions within the WGC. Heat transport along this coast does not explain the differences in lateral heat advection between simulations as heat must be advected from this current system into the interior of the Labrador Sea.

We suspect that the combination of heat transport within the water mass as well as eddy processes along the western coast of Greenland can address the differences in lateral heat flux. Figure 4 shows the 2004–2015 spatially averaged EKE as computed from AVISO observations and our five simulations. All simulations experience heightened EKE along the western coast of Greenland, suggesting the simulations do

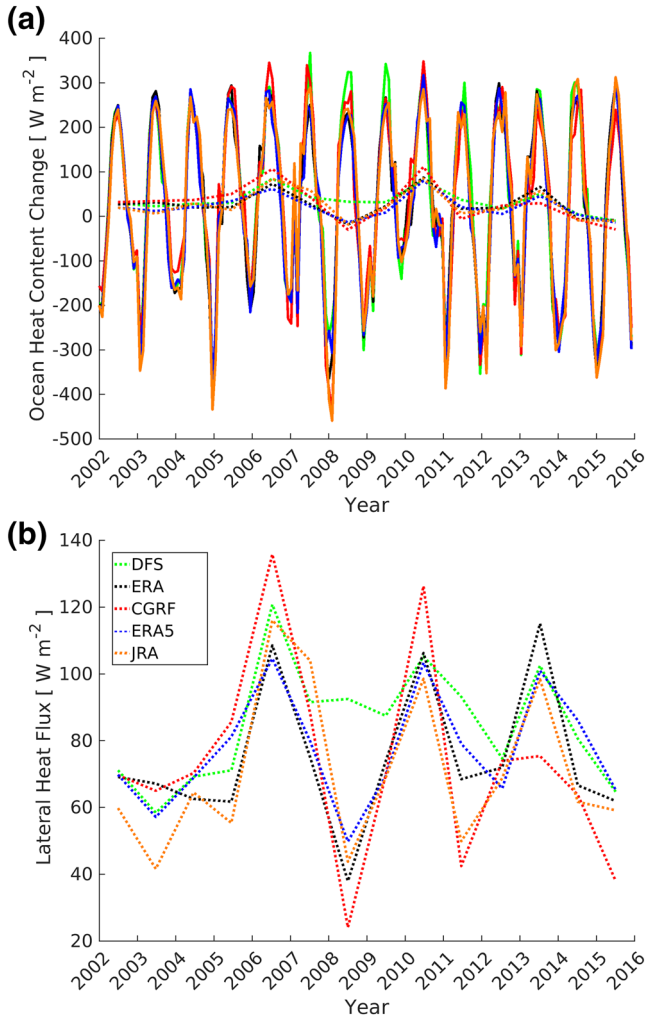

Figure 6. Monthly averaged (a) change in oceanic heat content and (b) lateral heat flux for each of the five simulations. Dotted lines indicate the yearly mean. Monthly values (solid line) were omitted from (b) for clarity. Values were spatially averaged over the red polygon in Figure 1(a).

produce some eddy fluxes in this region. Furthermore, the differences in the EKE field help explain the differences in lateral heat advection as described above. No single simulation appears to best represent the EKE along the western coast of Greenland. DFS, having a lower heat transport (Figure 7(a)), has greater EKE than the other simulations, suggesting that DFS may have higher heat transport via eddy processes from the WGC to the Labrador Sea. The CGRF simulation, having the highest heat transport within the Irminger Water mass south of Cape Farewell, has a larger spatial extent but lower EKE values which also occurs slightly further northwest compared to the other simulations, as well as reduced EKE in the interior Labrador Sea. This suggests that the larger amount of heat simulated within the Irminger Water layer for the CGRF simulation could be less likely to enter the interior of the Labrador Sea, leading to reduced lateral heat flux as detailed above. This is supported by greater heat transported north through Davis Strait (Table 3).

However, heat alone does not set the stratification. Freshwater has a larger impact on density at these latitudes; any freshwater within the EGC and WGC can also enter the interior of the Labrador Sea, increasing stratification. Figure 7(b) illustrates the freshwater transport ($S < 34.8$, $\rho_\theta < 1{,}027.68$ kg m^{-3}) that passes Cape Farewell and shows that the CGRF simulation has much more freshwater within this water mass than the remaining simulations. This freshwater resides above the Irminger Water mentioned above, and eddies that spawn from the WGC hold substantial surface freshwater which is carried toward the interior basin. CGRF, with sometimes nearly double the freshwater transport but less EKE compared to the remaining simulations, likely still transports more freshwater into the interior Labrador Sea, leading to a more stratified basin. While the lateral advection of heat and freshwater increases the stratification of the Labrador Sea throughout most of the year, the removal of heat from the ocean occurs during the extended convective wintertime.

3.4. Labrador Sea Water

With variations in the air–sea heat flux, as well as lateral transport of heat and freshwater, each simulation produced a Labrador Sea with slightly different properties. A spatial plot of the average March MLD is shown in Figure 8. With relatively few Argo floats in the Labrador Sea at any given time, the winter (January–March) maximum MLDs at the corresponding ANHA4 grid point are shown instead (Figure 8(f)). Low-resolution simulations often contain a mixed layer which is both too spacious and deep; a result of not resolving buoyant eddies produced within the WGC that enter the northern Labrador Sea (see model evaluation section). This promotes weaker stratification within the northern Labrador Sea, forcing deep mixing within this region that is not observed. This is clearly occurring for our five simulations (Figures 8(a)–(e)) as the Argo observations are confined to a much smaller region with shallower depths (maximum 1,800 m). The CGRF simulation, with the weakest surface heat loss, has the thinnest and least widespread MLD (1,600 m; Figure 8(c)). ERA5 has the strongest surface heat loss and the deepest mixed layer (2,000 m; Figure 8(d)). DFS (Figure 8(a)) has a larger spatial extent of its MLD, albeit slightly shallower than JRA (Figure 8(e)) and ERA5.

The combination of air–sea heat flux and freshwater changes due to precipitation and evaporation sets the total surface buoyancy flux (Figure 9(a)). While solar radiation (dotted line) supplies buoyancy, the nonsolar thermal fluxes including longwave radiation and other heat fluxes (dashed) removes far more. Processes that modify the sea surface salinity via precipitation or evaporation (dashed-dot) have similar values across the five simulations for the entire evaluation period. As the nonsolar thermal fluxes drive most of the variability in the net buoyancy flux, the input and removal of atmospheric freshwater between our simulations

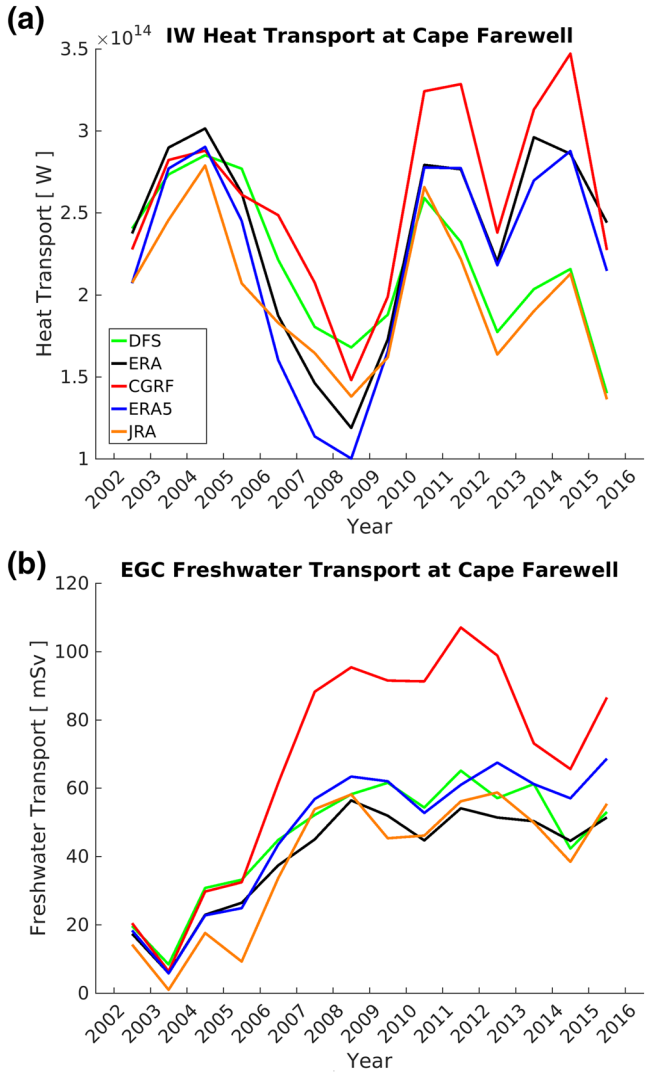

Figure 7. Water mass properties between Cape Farewell and the 2,500 m isobath to the south (Teal line; Figure1(a)). The westward heat transport for Irminger Water (IW: $T > 3.5$°C, $S > 34.8$, $\rho_\theta < 1{,}027.68$ kg m^{-3}) is shown in (a), while the westward freshwater transport (referenced to 34.8) associated with the East Greenland Current water mass (EGC: $S < 34.8$, $\rho_\theta < 1{,}027.68$ kg m^{-3}) is shown in (b).

is relatively minor. The DFS and JRA simulations often have the greatest net buoyancy loss but it is clearer where this arises from; JRA has reduced solar input while DFS has stronger heat loss via the nonsolar thermal term. A spatial comparison of the minimum grid point surface buoyancy gain is shown in S3, highlighting regional differences.

Finally exploring how the various surface buoyancy and lateral fluxes translate into changes at depth within the Labrador Sea, Figure 9(b) illustrates the convective energy which must be removed such that the water column is neutrally stratified to 2,000 m. Simulations all present similar interannual variability with the weakest stratification simulated during the winters of 2008, 2012, 2014, and 2015. The JRA and DFS simulations, with the greatest buoyancy losses, are often the most weakly stratified simulations. Conversely, the CGRF simulation had the least buoyancy loss and tended to have the strongest stratification throughout the integration period. This is further exacerbated by the additional freshwater carried by the CGRF simulation within the EGC/WGC (Figure 7(b)). We note that the ERA and ERA5 simulations start to deviate from the other simulations around 2010 when the WGC starts transporting more heat for these simulations (Figure 7(a)). This heat, and CGRF's additional freshwater, will partially enter the interior Labrador Sea, increasing stratification.

The MLD (Figure 9(c)) appears inverse to the convective energy, though the mixed layer gives understanding on how deep convection penetrates down to rather than how stratified the Labrador Sea is. The simulations overestimated the MLD when compared against Argo observations while matching the observed interannual variability. This interannual variability is closely linked to the NAO index (see Yashayaev & Loder, 2016; their Figure 5). Years with a deep mixed layer (2008, 2012, and 2014–2015) have strongly positive NAO, while the opposite occurs for years with negative NAO (i.e., 2010). Both the DFS and JRA simulations tended to have the deepest mixed layer. MLDs provide some information on the depth of convection, though they do not convey any information on the volume or density class of LSW.

The two components of LSW, ULSW and CLSW, are produced during periods of deep convection (Figure 10). Our calculated density range of LSW (Figure 10(a)) shows that the CGRF simulation has the lowest density while DFS and JRA have the densest, in line with the amount of buoyancy loss detailed above. This subfigure also shows that each simulation is slowly becoming more dense in our region of interest, highlighting numerical drift. LSW layer thicknesses deviate between simulations within 1 year of integration. Not only does the CGRF simulation have less dense LSW, it also forms thinner ULSW (Figure 10(b)) and CLSW (Figure 10(c)) layers, producing a thinner overall LSW layer (Figure 10(d)). The DFS (JRA) simulation often held the thickest LSW layer, likely a product of enhanced (reduced) buoyancy loss (gain). While each simulation shows the ULSW/CLSW layer thickness changes up to 600 m between years, the total LSW layer thickness (Figure 10(d)) only changes by up to 200 m if we ignore the first couple years that could be considered an adjustment phase from the initial conditions. Much of this layer thickness change is the conversion of ULSW into CLSW (or vice versa), as Kieke et al. (2006) showed with a correlation of -0.85. However, our five simulations did not correlate that strongly, with the DFS simulation at -0.53, CGRF at -0.47, JRA at -0.47, ERA at -0.46, and ERA5 at -0.43. We suspect that our method of classifying LSW with a moving density as determined by subduction rate played a strong role here. Other methods to determine LSW density range were carried out, though we settled on the above option as it factored in density drift and maintained an accurate representation of the layer thickness.

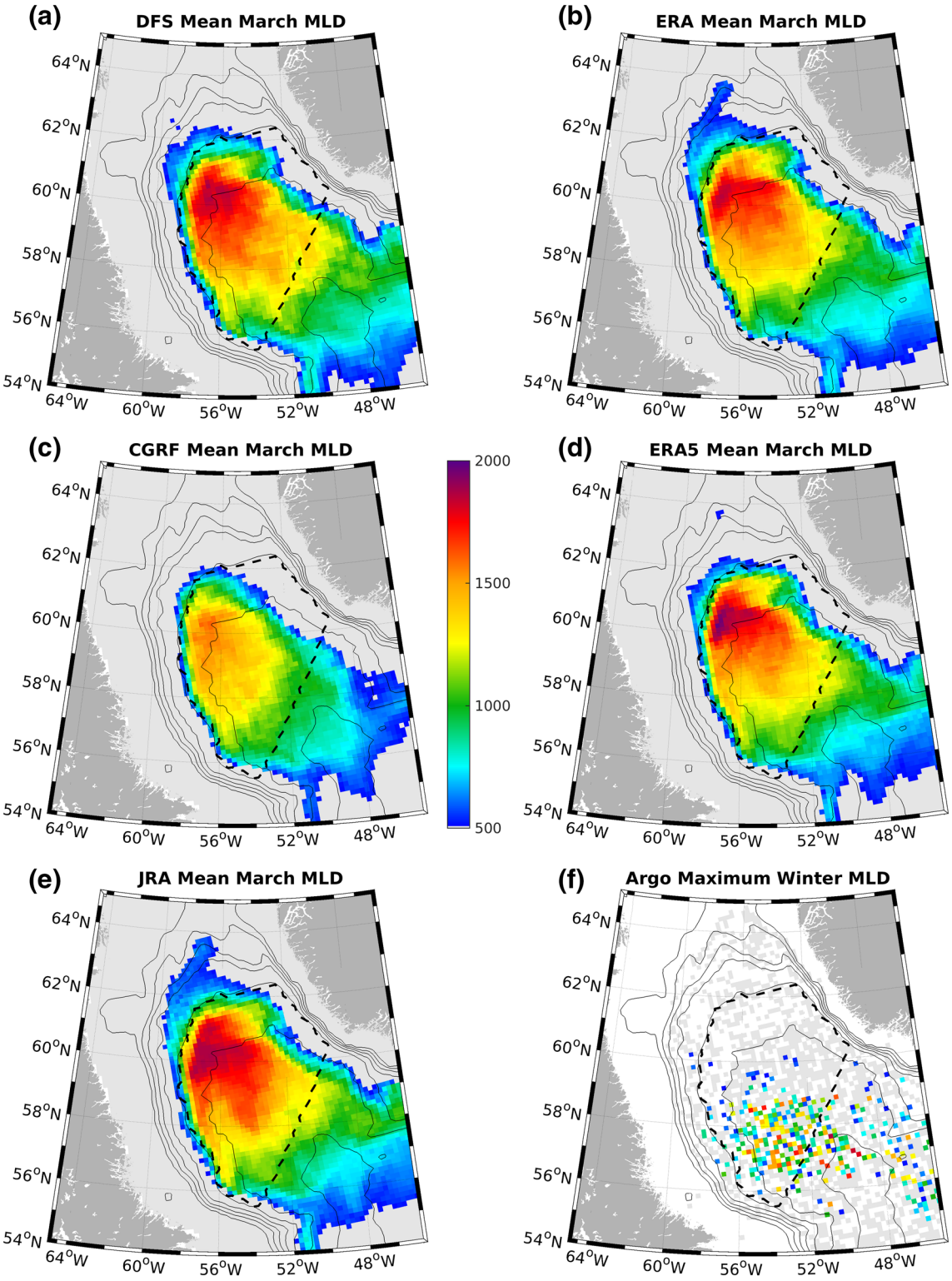

Figure 8. Shaded colors indicate the 2002–2015 mean March mixed layer depth (MLD), in meters, for each simulation (a–e). Observed ARGO data showing the maximum grid point winter (January–March) MLD from 2002 to 2015 are shown in (f) where whitespace indicates no data. Light gray indicates a MLD less than 500 m. Bathymetric contours of 500 m are indicated by the solid black lines while the dashed black line indicates the red polygon in Figure 1(a).

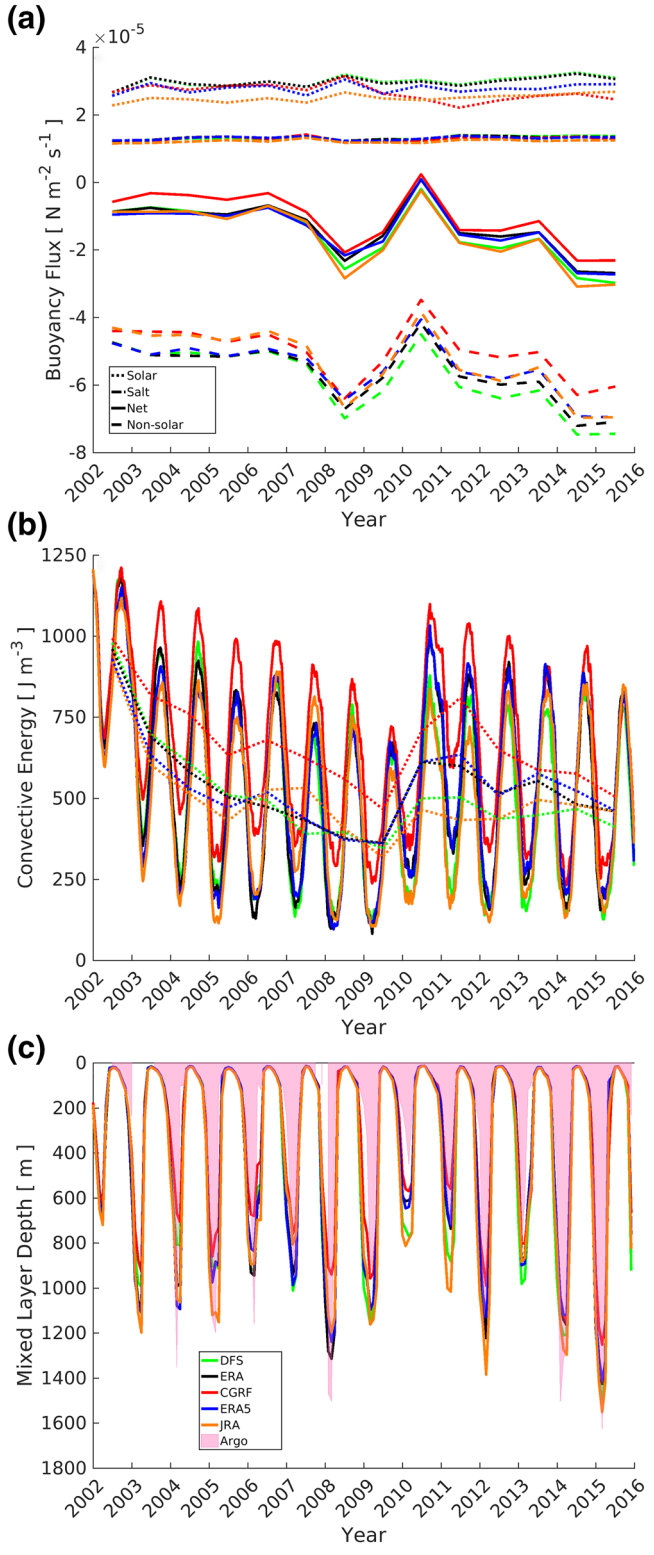

Figure 9. Averaged (a) yearly solar, nonsolar thermal, and precipitation minus evaporation surface buoyancy fluxes, (b) monthly convective energy values to a reference depth of 2,000 m, and (c) monthly mixed layer depths with ARGO observations for the five simulations. Dotted lines in (b) indicate the yearly mean. Values were spatially averaged over the red polygon in Figure 1(a).

LSW thickness does not quite give enough information to determine the volume of LSW produced, which we calculate by a kinematic subduction approach (Equation 4). The lateral advection term, opaque in Figure 11, shows primarily a positive contribution to the net subduction across the time series. The vertical motion of the mixed layer, translucent in this figure, always shows positive subduction. The vertical advection term was between 1 and 2 orders of magnitude lower and is not displayed nor discussed further. While some simulations held greater subduction rates (e.g., ERA during 2014), they did not always have the densest value. This implies that strong subduction rate does not indicate denser LSW. No one simulation had the greatest subduction rate across the years, though the simulations with stronger buoyancy loss (DFS and JRA) more often had the densest LSW. Conversely, the simulation with the weakest buoyancy loss (CGRF) also had the least dense LSW. While numerical drift slowly caused LSW to increase in density, the CGRF simulation was closest to the observed value, often within the density range of observed LSW (1,027.68–1,027.80 kg m^{-3}) as discussed above.

4. Discussion and Conclusion

This sensitivity study involved forcing an ocean model with five different atmospheric forcing data sets to evaluate the ocean's response over a portion of the Labrador Sea primarily in regards to the production of LSW. The five data sets in question, ERA5, DFS5.2, ERA-Interim, JRA55-do, and CGRF, showed similar interannual variability across their forcing fields, though the small differences in each data set resulted in varying levels of yearly averaged air–sea heat loss, at 58.5, 53.4, 51.0, 47.9, and 46.6 W m^{-2}, respectively. ERA5 had the strongest heat loss but not the strongest surface buoyancy loss. Precipitation and evaporation, while significantly different among the forcing data sets, provided minimal difference in salinity-driven surface buoyancy flux. The DFS and JRA simulations extracted the most buoyancy from the Labrador Sea: DFS from stronger turbulent heat fluxes while JRA maintained strong buoyancy loss via a reduction in solar radiation. Our simulations were eddy permitting and only small EKE differences are noted between the five simulations. We attribute these differences to wind speed frequency and strength within the atmospheric data sets, as well as baroclinic changes induced within the boundary currents. Eddies are very important in the Labrador Sea but numerical simulations require higher resolution to adequately resolve them (Rieck et al., 2019). We suspect that our conclusions will hold true for simulations with higher resolution, although future work is needed to confirm this.

We find that simulations with slightly stronger surface buoyancy loss experience greater MLDs (up to 300 m). With greater MLDs, the LSW layer thickness is also greater (up to 300 m). The maximum density of LSW which subducted the mixed layer is correlated to the surface buoyancy loss, leading to simulations with stronger forcing to produce denser LSW. However, the subduction volume associated with this density does not appear to be strongly influenced by small changes in the surface buoyancy flux. This apparent contrast to the above as the LSW layer thickness indicates that there must be a larger volume of LSW produced with stronger surface buoyancy loss but not at the

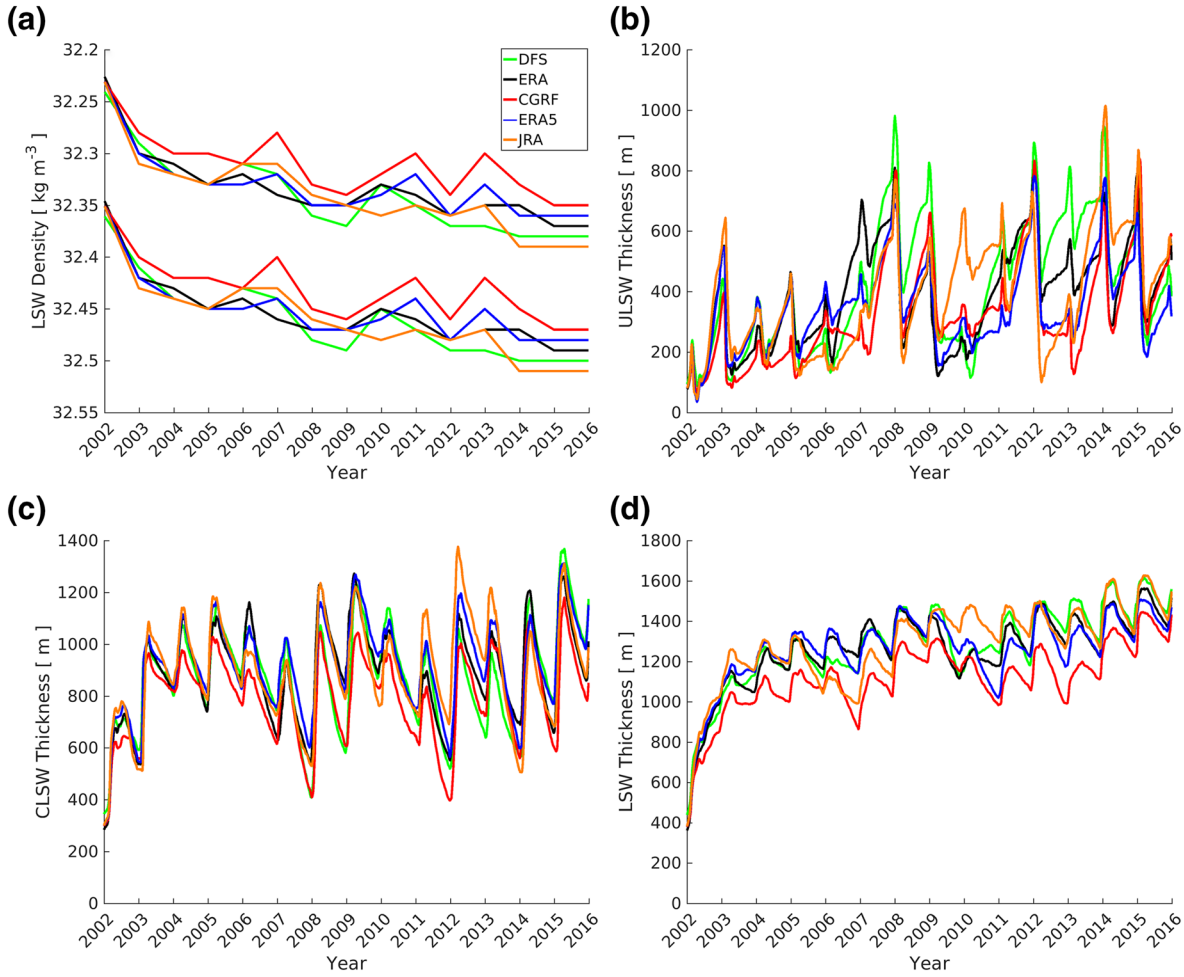

Figure 10. Upper and lower yearly density (referenced to 1,000 dbar) values of LSW are shown in (a). Monthly average layer thicknesses of Upper Labrador Sea Water (ULSW, (b)), Classical Labrador Sea Water (CLSW, (c)), and combined (d) are shown for each of the five simulations. Values were spatially averaged over the red polygon in Figure 1(a).

greatest density. We attribute this to a larger spatial extent of deep convection (Figure 8) which would increase the overall LSW layer thickness.

Our results fit with those from Chaudhuri et al. (2016) who performed a similar sensitivity study. They forced an ocean model with four reanalysis products and found the largest changes occurred within the top 1,000 m, though areas with deep convection saw significant differences at great depths. They attributed this to either differences in wind speed or heat flux, both of which we show exist between forcing products over the Labrador Sea. Garcia-Quintana et al. (2019) took this further by dramatically reducing precipitation. Reducing precipitation to one third of the original value resulted in a substantial densification of LSW, though the reduction in sensible heat flux was only about 1–2 W m^{-2}. While our above results have much larger heat loss changes, Garcia-Quintana et al. (2019) had a larger change in subduction density than what we found, indicating that the freshwater addition via precipitation impacts the stratification far stronger than the sensible and latent heat flux associated with precipitation. However, our CGRF and JRA simulations had much less precipitation than the other forcing sets (Figure 3), but the surface buoyancy flux differences between these simulations and the others were minor compared to the other sources of buoyancy flux (Figure 9(a)).

Considering how strong the turbulent air–sea heat fluxes are, it is not surprising that both Garcia-Quintana et al. (2019) and Holdsworth and Myers (2015) had a reduction in the MLD, subduction rate, and density of LSW when they filtered high-frequency events from their atmospheric forcing. Bramson (1997) ran a series

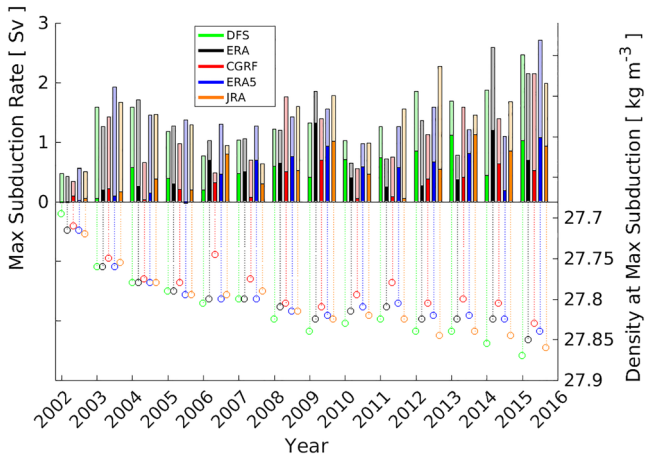

Figure 11. Yearly maximum subduction rate (bars) along with the density for this maximum subduction rate (stems) for each of the five simulations within the red polygon in Figure 1(a). Subduction is categorized into two terms: lateral advection (opaque bars) and movement of the mixed layer (translucent bars). Vertical advection was negligible and is not shown. The horizontal axis illustrates discrete years and not monthly values of subduction.

of sensitivity experiments varying heat flux components and identified changes in the air–sea fluxes clearly result in modifications to the MLD. From our five simulations, we also found that the MLD, subduction rate, and density are all modified from variations in surface forcing.

The atmospheric data sets used in our study are relatively common products to force hindcast ocean simulations. The above sensitivity studies by Bramson (1997), Holdsworth and Myers (2015), and Garcia-Quintana et al. (2019) often used realistic forcing which was perturbed to such a state that was no longer realistic. While they all found LSW production was influenced by atmospheric forcing, we show that relatively small changes in forcing can impact LSW production rate and density. Such differences in forcing and resulting density of LSW identify that a traditional static density criteria for LSW classification may not be suitable. Simulations which use slightly stronger/weaker forcing may produce deep water within the Labrador Sea which is too dense/light to be considered LSW by such a traditional method. The method used here, a moving density scale, showed success at the interannual variability of LSW formation rate for five simulations with different atmospheric forcing. This is further exacerbated by numerical drift.

Our simulations suffer from numerical drift, a seemingly unavoidable consequence of modeling within the Labrador Sea (Marzocchi et al., 2015; Rattan et al., 2010). Numerical drift does not appear sensitive to the model's configuration as Rattan et al. (2010) showed with similar drift between regional and global configurations. Our simulations' drift prevented us from using standard LSW density ranges (potential density 1,027.68–1,027.80) as later years were producing deep water denser than LSW. Using a technique to classify LSW using moving density definition allowed a far more useful analysis on these simulations. Our LSW density and thickness steadily increase over time while observations suggest that LSW density has been slowly decreasing (Kieke & Yashayaev, 2015). However, our simulations match well against Argo observations of the mixed layer, highlighting that simulations with numerical drift can still have accurate aspects. Lower-resolution simulations that suffer from numerical drift have long been a useful tool to understand climate scenarios even with their shortcomings.

Our results show the relative impact of each of the air–sea heat flux terms within the Labrador Sea. The radiative and turbulent terms are the dominating source of air–sea heat flux, though the remaining terms should not be ignored. While our results suggest that an additional 1–12 W m^{-2} of surface heat loss produce a deeper mixed layer and denser LSW, our simulations had significant differences in the lateral freshwater and heat fluxes that govern the restratification rate. With lateral heat fluxes that differed between simulations of up to 15 W m^{-2}, the choice of atmospheric forcing strongly influenced the lateral restratification rate in the Labrador Sea as well as the surface buoyancy forcing. We speculate the additional lateral buoyancy flux was likely due to upstream changes within the Irminger Basin and Arctic, judging from the heat and freshwater transport in Figure 7. Putting these heat flux values into perspective, the Representative Concentration Pathways simulations project the anthropogenic influence on the Earth's Climate range from 2.6 to 8.5 W m^{-2} (Riahi et al., 2007; Van Vuuren et al., 2007) while our planet is currently experiencing an additional 1-3 W m^{-2} of heating since before the industrial revolution (IPCC, 2014). However, these heat flux values are averaged over the entire planet, not just the Labrador Sea, and while each region will experience some variability in additional heating, we show that a large impact occurs when exposed to a similar magnitude change in heat flux.

As these atmospheric data sets are used to drive ocean simulations and we show that the small differences between realistic atmospheric data sets produce significant changes within the Labrador Sea, ocean modelers should take caution with the forcing product they use. While we only investigated how the variability influenced production and density of LSW, many other regions are likely to be influenced by such variability between data sets. Long ocean simulations may be particularly sensitive to such differences, as a few additional watts supplied over the course of decades may produce very different, and perhaps unrealistic, results.

Data Availability Statement

We also appreciate the data provided by the International Argo Program.

Acknowledgments
We would like to thank Yarisbel Garcia-Quintana for her help on calculating subduction. We are grateful to the NEMO and development team and the DRAKKAR project for providing the model and continuous guidance, and to Westgrid and Compute Canada for computational resources to perform our simulations as well as archival of model experiments (http://www.computecanada.ca). This work was supported by NSERC (grant number RGPCC 433898) as well as an NSERC Discovery grant (grant number RGPIN 04357). No conflicts of interest exist to report of.

References

Bamber, J., van den Broeke, M., Ettema, J., Lenaerts, J., & Rignot, E. (2012). Recent large increases in freshwater fluxes from Greenland into the North Atlantic. *Geophysical Research Letters*, *39*, L19501. https://doi.org/10.1029/2012GL052552

Benetti, M., Reverdin, G., Yashayaev, I., Holliday, N. P., Tynan, E., Torres-Valdes, S., et al. (2017). Composition of freshwater in the spring of 2014 on the southern Labrador shelf and slope. *Journal of Geophysical Research: Oceans*, *122*, 1102–1121. https://doi.org/10.1002/2016JC012244

Böning, C. W., Behrens, E., Biastoch, A., Getzlaff, K., & Bamber, J. L. (2016). Emerging impact of Greenland meltwater on deepwater formation in the North Atlantic Ocean. *Nature Geoscience*, *97*(7), 523–527.

Bramson, L. S. (1997). *Air–sea interactions and deep convection in the Labrador Sea* (MS thesis, 115 pp.). Department of Oceanography. California, USA: Naval Postgraduate School.

Brossier, C. L., Béranger, K., & Drobinski, P. (2012). Sensitivity of the northwestern Mediterranean Sea coastal and thermohaline circulations simulated by the 1/12°-resolution ocean model NEMO-MED12 to the spatial and temporal resolution of atmospheric forcing. *Ocean Modelling*, *43–44*, 94–107.

Chanut, J., Barnier, B., Large, W., Debreu, L., Penduff, T., Molines, J. M., & Mathiot, P. (2008). Mesoscale eddies in the Labrador Sea and their contribution to convection and restratification. *Journal of Physical Oceanography*, *28*(8), 1617–1643.

Chaudhuri, A. H., Ponte, R. M., & Forget, G. (2016). Impact of uncertainties in atmospheric boundary conditions on ocean model solutions. *Ocean Modelling*, *100*, 96–108.

Condron, A., & Renfrew, I. A. (2013). The impact of polar mesoscale storms on northeast Atlantic Ocean circulation. *Nature Geoscience*, *6*(1), 34–37.

Courtois, P., Hu, X., Pennelly, C., Spence, P., & Myers, P. G. (2017). Mixed layer depth calculation in deep convection regions in ocean numerical models. *Ocean Modelling*, *120*, 60–78.

Cuny, J., Rhines, P. B., Niiler, P. P., & Bacon, S. (2002). Labrador Sea boundary currents and the fate of the Irminger Sea Water. *Journal of Physical Oceanography*, *32*(2), 627–647.

Curry, B., Lee, C. M., & Petrie, B. (2011). Volume, freshwater, and heat fluxes through Davis Strait, 2004-05. *Journal of Physical Oceanography*, *41*(3), 429–436.

Curry, B., Lee, C. M., Petrie, B., Moritz, R. E., & Kwok, R. (2014). Multiyear volume, liquid freshwater, and sea ice transports through Davis Strait, 2004–10. *Journal of Physical Oceanography*, *44*(4), 1244–1266.

Curry, R. G., McCartney, M. S., & Joyce, T. M. (1998). Oceanic transport of subpolar climate signals to mid-depth subtropical waters. *Nature*, *391*(6667), 575–577.

Dai, A., Qian, T., Trenberth, K. E., & Milliman, J. D. (2009). Changes in continental freshwater discharge from 1948 to 2004. *Journal of Climate*, *22*(10), 2773–2792.

Dee, D. P., Uppala, S. M., Simmons, A. J., Berrisford, P., Poli, P., Kobayashi, S., et al. (2011). The ERA-Interim reanalysis: Configuration and performance of the data assimilation system. *Quarterly Journal of the Royal Meteorological Society*, *137*, 553–597.

De Jong, M. F., Bower, A. S., & Furey, H. H. (2016). Seasonal and interannual variations of Irminger ring formation and boundary-interior heat exchange in FLAME. *Journal of Physical Oceanography*, *46*(6), 1717–1734.

Dickson, R., Rudels, B., Dye, S., Karcher, M., Meincke, J., & Yashayaev, I. (2007). Current estimates of freshwater flux through Arctic and subarctic seas. *Progress in Oceanography*, *73*(3–4), 210–230.

Drinkwater, K. F. (1988). On the mean and tidal currents in Hudson Strait. *Atmosphere-Ocean*, *26*(2), 252–266.

Dussin, R., Barnier, B., & Brodeau, L. (2016). *The making of Drakkar Forcing Set DFS5*. Grenoble, France: LGGE.

Duvivier, A. K., Cassano, J. J., Craig, A., Hamman, J., Maslowski, W., Nijssen, B., et al. (2016). Winter atmospheric buoyancy forcing and oceanic response during String Wind Events around Southeastern Greenland in the Regional Arctic System Model (RASM) for 1990–2010. *Journal of Climate*, *29*(3), 975–994.

Ferry, N., Parent, L., Garric, G., Barnier, B., & Jourdain, N. C. (2010). Mercator global eddy permitting ocean reanalysis GLORYS1V1: Description and results. *Mercator-Ocean Quarterly Newsletter*, *36*, 15–27.

Feucher, C., Garcia-Quintana, Y., Yashayaev, I., Hu, X., & Myers, P. G. (2019). Labrador Sea Water formation rate and its impact on the local Meridional Overturning Circulation. *Journal of Geophysical Research: Oceans*, *124*, 5654–5670. https://doi.org/10.1029/2019JC015065

Fichefet, T., & Maqueda, M. A. M. (1997). Sensitivity of a global sea ice model to the treatment of ice thermodynamics and dynamics. *Journal of Geophysical Research*, *102*(C6), 12609–12646.

Garcia-Quintana, Y., Courtois, P., Hu, X., Pennelly, C., Kieke, D., & Myers, P. G. (2019). Sensitivity of Labrador Sea Water formation to changes in model resolution, atmospheric forcing, and freshwater input. *Journal of Geophysical Research: Oceans*, *124*, 2126–2152. https://doi.org/10.1029/2018JC014459

Gelderloos, R., Katsman, C. A., & Drijfhout, S. S. (2011). Assessing the roles of three eddy types in restratifying the Labrador Sea after deep convection. *Journal of Physical Oceanography*, *41*(11), 2102–2119.

Gelderloos, R., Straneo, F., & Katsman, C. A. (2012). Mechanisms behind the temporary shutdown of deep convection in the Labrador Sea: Lessons from the great salinity anomaly years 1968–71. *Journal of Climate*, *25*(19), 6743–6755.

Gillard, L., Hu, X., Myers, P. G., & Bamber, J. L. (2016). Meltwater pathways from marine terminating glaciers of the Greenland ice sheet. *Geophysical Research Letters*, *43*, 10873–10881. https://doi.org/10.1002/2016GL070969

Hersbach, H., & Dee, D. J. E. N. (2016). ERA5 reanalysis is in production. *ECMWF Newsletter*, *147*(7), 5–6.

Holdsworth, A. M., & Myers, P. G. (2015). The influence of high-frequency atmospheric forcing on the circulation and deep convection of the Labrador Sea. *Journal of Climate*, *28*(12), 4980–4996.

Holte, J., & Talley, L. (2009). A new algorithm for finding mixed layer depths with applications to Argo data and Subantarctic Mode Water formation. *The Journal of Atmospheric and Oceanic Technology*, *26*(9), 1920–1939.

Hurrell, J. W. (1995). Decadal trends in the North Atlantic Oscillation: Regional temperatures and precipitation. *Science*, *269*(5224), 676–679.

Hurrell, J. W., & Deser, C. (2010). North Atlantic climate variability: The role of the North Atlantic Oscillation. *Journal of Marine Systems*, *78*, 28–41.

IPCC. (2014). Climate change 2014: Synthesis report. In Core Writing Team, R. K. Pachauri, & L. A. Meyer (Eds.), *Contribution of working groups I, II, and III to the fifth assessment report of the Intergovernmental Panel on Climate Change* (51 pp.). Geneva, Switzerland: IPCC.

Jung, T., Serrar, S., & Wang, Q. (2014). The oceanic response to mesoscale atmospheric forcing. *Geophysical Research Letters*, *41*, 1255–1260. https://doi.org/10.1002/2013GL059040

Kieke, D., Rhein, M., Stramma, L., Smethie, W. M., LeBel, D. A., & Zenk, W. (2006). Changes in the CFC inventories and formation rates of Upper Labrador Sea Water, 1997–2001. *Journal of Physical Oceanography*, *36*(1), 64–86.

Kieke, D., & Yashayaev, I. (2015). Studies of Labrador Sea Water formation and variability in the subpolar North Atlantic in the light of international partnership and collaboration. *Progress in Oceanography*, *132*, 220–232. https://doi.org/10.1016/j.pocean.2014.12.010

Lab Sea Group. (1998). The Labrador Sea deep convection experiment. *The Bulletin of the American Meteorological Society*, *79*(10), 2033–2058.

Large, W. G., & Yeager, S. G. (2008). The global climatology of an interannually varying air–sea flux data set. *Climate Dynamics*, *33*(2–3), 341–364.

Lazier, J., Hendry, R., Clarke, A., Yashayaev, I., & Rhines, P. (2002). Convection and restratification in the Labrador Sea, 1990–2000. *Deep Sea Research I: Oceanographic Research Papers*, *49*(10), 1819–1835.

Li, F., Lozier, M. S., Danabasoglu, G., Holliday, N. P., Kwon, Y.-O., Romanou, A., et al. (2019). Local and downstream relationships between Labrador Sea Water volume and North Atlantic Meridional Overturning Circulation variability. *Journal of Climate*, *31*(13), 3883–3898.

Lindsay, R., Wensnahan, M., Schweiger, A., & Zhang, J. (2014). Evaluation of seven different atmospheric reanalysis products in the Arctic. *Journal of Climate*, *27*(3), 2588–2606.

Lozier, M. S., Li, F., Bacon, S., Bahr, F., Bower, A. S., Cunningham, S. A., et al. (2019). A sea change in our view of overturning in the subpolar North Atlantic. *Science*, *363*(6426), 516–521.

Madec, G. (2008). *Note du Pôle de modélisation* (No. 27, ISSN No. 1288-1619). France: Institut Pierre-Simon Laplace (IPSL).

Marshall, J., & Schott, F. (1999). Open-ocean convection: Observations, theory, and models. *Reviews of Geophysics*, *37*(1), 1–64.

Marzocchi, A., Hurshi, J. J. M., Holiday, N. P., Cunningham, S. A., Blaker, A. T., & Coward, A. C. (2015). The North Atlantic subpolar circulation in an eddy-resolving global ocean model. *Journal of Marine Systems*, *142*, 126–143.

McGeehan, I., & Maslowski, W. (2011). Impact of shelf-basin freshwater transport on deep convection in the western Labrador Sea. *Journal of Physical Oceanography*, *41*(11), 2187–2210.

Moore, G. W. K., Pickart, P. S., & Renfrew, I. A. (2011). Complexities in the climate of the subpolar North Atlantic: A case study from the winter of 2007. *Quarterly Journal of the Royal Meteorological Society*, *137*(656), 757–767.

Moore, G. W. K., Pickart, R. S., Renfrew, I. A., & Våge, K. (2014). What causes the location of the air–sea turbulent heat flux maximum over the Labrador Sea? *Geophysical Research Letters*, *41*, 3628–3635. https://doi.org/10.1002/2014GL059940

Müller, V., Kieke, D., Myers, P. G., Pennelly, C., & Mertens, C. (2017). Temperature flux carried by individual eddies across 47°N in the Atlantic Ocean. *Journal of Geophysical Research: Oceans*, *122*, 2441–2464. https://doi.org/10.1002/2016JC012175

Myers, P. (2005). Impact of freshwater from the Canadian Arctic Archipelago on Labrador Sea Water formation. *Geophysical Research Letters*, *32*, L06605. https://doi.org/10.1029/2004GL022082

Myers, P. G., Donnelly, C., & Ribergaard, M. H. (2009). Structure and variability of the West Greenland Current in Summer derived from 6 repeat standard sections. *Progress in Oceanography*, *80*(1–2), 93–112.

Myers, P. G., Kulan, N., & Ribergaard, M. H. (2007). Irminger Water variability in the West Greenland Current. *Geophysical Research Letters*, *34*, L17601. https://doi.org/10.1029/2007GL030419

Pickart, R. S., & Spall, M. A. (2007). Impact of Labrador Sea convection on the North Atlantic Meridional Overturning Circulation. *Journal of Physical Oceanography*, *37*(9), 2207–2227.

Pickart, R. S., Torres, D. J., & Clarke, R. A. (2002). Hydrography of the Labrador Sea during active convection. *Journal of Physical Oceanography*, *32*(2), 428–457.

Pillar, H. R., Johnson, H. L., Marshall, D. P., Heimbach, P., & Takao, S. (2018). Impacts of atmospheric reanalysis uncertainty on Atlantic overturning estimates at 25°N. *Journal of Climate*, *31*(21), 8719–8744.

Raasch, S., & Etling, D. (1997). Modeling deep ocean convection: Large eddy simulation in comparison with laboratory experiments. *Journal of Physical Oceanography*, *28*(9), 1786–1802.

Rattan, S., Myers, P. G., Trequier, A. M., Theetten, S., Biastoch, A., & Böning, C. (2010). Toward an understanding of Labrador Sea salinity drift in eddy-permitting simulations. *Ocean Modelling*, *35*(102), 77–88.

Renfrew, I. A., Moore, G. W. K., Guest, P. S., & Bumke, K. (2002). Comparison of surface layer and surface turbulent flux observations over the Labrador Sea with ECMWF analysis and NCEP reanalysis. *Journal of Physical Oceanography*, *32*, 383–400.

Rhein, M., Kieke, D., & Steinfeldt, R. (2015). Advection of North Atlantic Deep Water from the Labrador Sea to the southern hemisphere. *Journal of Geophysical Research: Oceans*, *120*, 2471–2487. https://doi.org/10.1002/2014JC010605

Riahi, K., Grübler, A., & Nakicenovic, N. (2007). Scenarios of long-term socio-economic and environmental development under climate stabilization. *Technical Forecasting and Social Change*, *74*, 887–935.

Ridenour, N., Hu, X., Jafarikhasragh, S., Landy, J. C., Lukovich, J. V., Stadnyk, T. A., et al. (2019). Sensitivity of freshwater dynamics to ocean model resolution and river discharge forcing in the Hudson Bay Complex. *Journal of Marine Systems*, *196*, 48–64.

Rieck, J. K., Böning, C. W., & Getzlaff, J. (2019). The nature of eddy kinetic energy in the Labrador Sea: Different types of mesoscale eddies, their temporal variability, and impact on deep convection. *Journal of Physical Oceanography*, *49*(8), 2075–2094.

Rykova, T., Straneo, F., & Bower, A. S. (2015). Seasonal and interannual variability of the West Greenland Current System in the Labrador Sea in 1993–2008. *Journal of Geophysical Research: Oceans*, *120*, 1318–1332. https://doi.org/10.1002/2014JC010386

Sathiyamoorthy, S., & Moore, G. W. K. (2002). Buoyancy flux at ocean weather station Bravo. *Journal of Physical Oceanography*, *32*(2), 458–474.

Schmidt, S., & Send, U. (2007). Origin and composition of seasonal Labrador Sea freshwater. *Journal of Physical Oceanography*, *37*(6), 1445–1454.

Schulze, L. M., & Frajka-Williams, E. (2018). Wind-driven transport of fresh shelf water into the upper 30 m of the Labrador Sea. *Ocean Science*, *14*(5), 1247–1264.

Schulze, L. M., Pickart, R. S., & Moore, G. W. K. (2016). Atmospheric forcing during active convection in the Labrador Sea and its impact on mixed-layer depth. *Journal of Geophysical Research: Oceans*, *121*, 6978–6992. https://doi.org/10.1002/2015JC011607

Smith, G. C., Roy, F., Mann, P., Dupont, F., Brasnett, B., Lemieux, J. F., et al. (2014). A new atmospheric dataset for forcing ice-ocean models: Evaluation of reforecasts using the Canadian global deterministic prediction system. *Quarterly Journal of the Royal Meteorological Society*, *140*(680), 881–894.

Spall, M. A. (2004). Boundary currents and watermass transformation in marginal seas. *Journal of Physical Oceanography*, *34*(5), 1197–1213.

Straneo, F. (2006). Heat and freshwater transport through the central Labrador Sea. *Journal of Physical Oceanography*, *36*(4), 606–628.

Straneo, F., & Saucier, F. (2008a). *The arctic–subarctic exchange through Hudson Strait*. In Arctic–subarctic ocean fluxes (pp. 249–261). Dordrecht, The Netherlands: Springer.

Straneo, F., & Saucier, F. (2008b). The outflow from Hudson Strait and its contribution to the Labrador Current. *Deep Sea Research Part I: Oceanographic Research Papers*, *55*(8), 926–646.

Tsujino, H., Urakawa, S., Nakano, H., Small, R. J., Kim, W. M., Yeager, S. G., et al. (2018). JRA-55 based surface dataset for driving ocean-sea-ice models (JRA55-do). *Ocean Modelling*, *130*, 79–139.

Van Vuuren, D. P., den Elzen, M. G. L., Lucas, P. L., Eickhout, B., Strengers, B. J., van Ruijven, B., et al. (2007). Stabilizing greenhouse gas concentrations at low levels: An assessment of reduction strategies and costs. *Climate Change*, *81*, 119–159.

Van Vuuren, D. P., Edmonds, J., Kainuma, M., Riahi, K., Thomson, A., Hibbard, K., et al. (2011). The Representative Concentration Pathways: An overview. *Climate Change*, *109*(1–2), 5 pp.

Wilson, C., Harle, J., & Wakelin, S. (2019). *Development of a regional ocean model for the Caribbean, including 3D dynamics, thermodynamics and full surface flu forcing* (National Oceanography Center Research and Consultancy Report, No. 65, 40 pp.). UK: National Oceanography Centre.

Yashayaev, I., & Loder, J. W. (2016). Recurrent replenishment of Labrador Sea Water and associated decadal-scale variability. *Journal of Geophysical Research: Oceans*, *121*, 8095–8814. https://doi.org/10.1002/2016JC012046

Yashayaev, I., & Loder, J. W. (2017). Further intensification of deep convection in the Labrador Sea in 2016. *Geophysical Research Letters*, *44*, 1429–1438. https://doi.org/10.1002/2016GL071668

Yashayaev, I., van Aken, H. M., Holliday, N. P., & Bersch, M. (2007). Transformation of the Labrador Sea Water in the subpolar North Atlantic. *Geophysical Research Letters*, *34*, L22605. https://doi.org/10.1029/2007GL031812

Yeager, S., & Danabasoglu, G. (2014). The origins of late-twentieth-century variations in the large-scale North Atlantic circulation. *Journal of Climate*, *27*(9), 3222–3247.